Journal of Computational Science 89 (2025) 102614

Contents lists available at ScienceDirect

Journal of Computational Science

journal homepage: www.elsevier.com/locate/jocs

Spatio-temporal consistency of cloud-microphysical parameter sensitivity in a warm-conveyor belt

Maicon Hieronymus [a],*, Annika Oertel [b], Annette K. Miltenberger [c], André Brinkmann [a]

[a] Institute of Computer Science, Johannes Gutenberg University, Anselm-Franz-von-Bentzel-Weg 12, 55128, Mainz, Germany
[b] Institute of Meteorology and Climate Research Troposphere Research (IMKTRO), Karlsruhe Institute of Technology (KIT), Karlsruhe, Germany
[c] Institute for Atmospheric Physics, Johannes Gutenberg University, Mainz, Germany

ARTICLE INFO

Dataset link: https://code.mpimet.mpg.de/projects/iconpublic

Keywords:
Sensitivity analysis
Warm conveyor belt
Cloud microphysics

ABSTRACT

A good representation of clouds and precipitation processes is essential in numerical weather and climate models. Subgrid-scale processes, such as cloud physics, are parameterized and inherently introduce uncertainty into models. Traditionally, the sensitivities of the model state to specific uncertain parameters are quantified through perturbations to a few selected parameters, limited by computational resources. Algorithmic Differentiation (AD) enables the efficient and simultaneous estimation of sensitivities for a large number of parameters, thereby overcoming the previous limitations and significantly enhancing the efficiency of the analysis. This framework provides an objective way to identify processes where more precise representations have the largest impact on model accuracy. AD-estimated sensitivities can also address the underdispersiveness of perturbed ensemble simulations by guiding the parameter selection or the perturbation itself. In our study, we applied AD to 169 uncertain parameters identified in the two-moment microphysics scheme of the numerical weather prediction (NWP) model ICON of the German Weather Service. This application of AD allowed us to evaluate the sensitivities of specific humidity, latent heating, and latent cooling along several thousand warm conveyor belt trajectories. This coherent, strongly ascending Lagrangian flow feature is crucial for the cloud and precipitation structure and the evolution of extratropical cyclones. The quantification of individual parameter sensitivities shows that only 38 parameters are of primary importance for the investigated model state variables. These parameters are associated with rain evaporation, hydrometeor diameter-mass relations, and fall velocities. Moreover, the parameter sensitivities systematically vary with different microphysical regimes, ascent behavior, and ascent stages of the WCB airstream. Finally, several parameters impact an extended region in the extratropical cyclone, illustrating the spatiotemporal consistency of cloud microphysical parameter uncertainty in the applied NWP model and microphysics scheme.

1. Introduction

Understanding and accurately predicting cloud properties and precipitation has been a focus of research for many years. The ability to accurately model these processes is essential for climate projections and numerical weather prediction (NWP). However, due to the small inherent spatial and temporal scales, cloud processes are subgrid-scale and, therefore, need to be represented by parameterizations, which inherently introduces uncertainty in NWP models. With the continuously increasing computer power, model resolutions of these models are steadily improving, increasing the importance of detailed bulk microphysics schemes. Operational weather services introduce physics perturbations in their ensemble prediction systems to account for uncertainty related to sub-grid-scale processes and their interaction with explicitly resolved dynamics. Examples of such perturbations are stochastically perturbed parameterization tendencies (SPPT) [1] or stochastically perturbed parameterizations (SPP) [2,3]. SPPT effectively simultaneously adds spatio-temporally correlated noise to several parametrized tendencies, implicitly assuming the same error characteristics for all perturbed parameterizations. This uniformity cannot reflect the true uncertainty associated with each specific parameter. Another downside is the violation of key conservation laws [4]. In contrast, SPP introduces random perturbations to a limited number of model parameters to account for uncertainty in the representation of subgrid-scale processes. This approach enables independent error characteristics but may lead to an underdispersive ensemble forecasting system [5,6].

* Corresponding author.
E-mail address: mhieronymus@uni-mainz.de (M. Hieronymus).

https://doi.org/10.1016/j.jocs.2025.102614
Received 19 December 2024; Received in revised form 21 March 2025; Accepted 9 May 2025
Available online 27 May 2025

Cloud microphysical and other parameterization schemes typically include hundreds of uncertain parameters. Sensitivity analyses, i.e., performing simulations with a range of different parameter values, are often performed to understand if and by how much specific parameter perturbations influence target variables, such as total surface precipitation, cloudiness, or characteristics of the large-scale flow. Sensitivity analysis is a powerful tool for quantifying the impact of parameters on a system's behavior. Providing information about the relevant parameters makes methods such as SPP more effective. However, exploring the phase space of uncertain parameters with full NWP simulations is very costly, and careful consideration of the ensemble design is needed to make the most of the computationally expensive simulations. Recently, perturbed parameter ensembles (PPEs) have been built for microphysical applications [7–12] facilitating a relatively dense sampling of a multi-parameter phase-space with a comparatively small number of NWP simulations. This method maintains the physical integrity and local conservation properties of the parametrization schemes. It also enables uncertainties to be depicted near their origins, potentially facilitating more targeted adjustments to the ensemble spread. Yet, the number of microphysical parameters in PPEs is typically fewer than ten, e.g., six parameters had been used by Frey et al. [11], and Johnson et al. [12] investigated the impact of ten parameters on twelve cloud properties. Those studies still require about 100 individual NWP simulations with high computational costs or statistical emulators.

Algorithmic Differentiation (AD) is a technique for efficiently and simultaneously calculating hundreds of instantaneous sensitivities at arbitrary time steps [13–15]. Thus, the entire uncertain parameter space can be covered simultaneously, and the sensitivity of selected target variables to the uncertain parameters can be quantified and compared. Bischof et al. [16] applied AD on the MM5 mesoscale modeling system. The tangent linear model created by AD is used to describe the evolution of errors or perturbations and to estimate the impact of additional observations in the initial temperature field. AD has been used in turbulence models by Bischof et al. [17] to assess the sensitivity of two models to their model parameters. Furthermore, Kim et al. [18] applied AD for atmospheric chemistry models to calculate the sensitivity of ozone to initial concentrations of 84 species and 178 reaction rate constants in different chemical regimes. As a last example, Gelbrecht et al. [19] discuss the usage of AD for earth system models to tune the models objectively and for online training of machine learning models as emulators. These emulators become more stable and accurate when gradients of the original model are used during online training [20–22].

Albeit enabling the quantification of instantaneous parameter sensitivities for a large number of parameters, the largest local gradients need not necessarily project on the strongest sensitivities of a strongly non-linear system, such as clouds and their interaction with flow dynamics. However, earlier investigations by Hieronymus et al. [13] suggest that the ordering of parameters, i.e., their relative importance, determined by AD carries some predictive power for the non-linear evolution of clouds.

WCBs are the primary cloud- and precipitation-producing airstreams in extratropical cyclones and substantially modify the mid-latitudes cloud radiative forcing. They typically ascend from the lower into the upper troposphere, where they can interact with the upper-level flow. Previous studies showed that uncertainty in the representation of diabatic heating along the ascending WCB airstream influences its cross-isentropic ascent strength [23–26] and the WCB ascent frequency [27]. Misrepresentation of WCB ascent in forecasts can subsequently influence the position of the upper-level ridge [24–26,28] and upper-level wind speed [29]. Considering the upscale error growth mechanism formulated by [30], WCBs are relevant for the cloud characteristics and surface precipitation and the large-scale flow evolution [31]. Latent heat release during cloud formation is the dominant diabatic heating contribution during WCB ascent [24,32,33].

Although cloud microphysics is the dominant diabatic heating source along WCB trajectories, few studies have systematically quantified parametric uncertainty in these large-scale weather systems, in contrast to, for example, convective systems for which sensitivities experiments have been performed more frequently [e.g.,9,12,34–38]. [39] applied perturbations to the terminal fall velocity of ice, deposition, and sublimation rates in a case study investigating an extratropical cyclone. They found that these parameters influence the mesoscale pattern of ice and liquid water content, relative humidity, and the formation of frontal rain bands. [40] researched how aerosols impact surface precipitation in North Pacific WCBs. While WCB trajectories strongly polluted with aerosols delay and reduce surface precipitation, the abundance of clean trajectories mitigates those effects.

In this study, we apply AD to quantify the microphysical parameter sensitivities of ICON's two-moment microphysics scheme [41,42] for specific humidity, latent heating, and latent cooling along warm conveyor belt trajectories from a convection-permitting simulation and, thus, identify the most relevant uncertain microphysical parameters. Specific humidity is interesting at lower layers due to its importance for cyclone dynamics. At the upper layers, namely the upper troposphere and lower stratosphere (UTLS), specific humidity determines the formation of cirrus clouds, which impacts the radiative forcing and surface temperature. Uncertainty in latent heating and cooling might lead to forecast busts [31] due to their role in cyclone dynamics, cross-isentropic ascent, potential vorticity, and the flow interaction at the upper layers [23–25,27] and are therefore of particular interest. Furthermore, the impact of cloud microphysics on large scales depends on the outflow height, which depends on latent heating and cooling. Specifically, we will address the following questions:

1. What are the key cloud microphysical uncertainties for specific humidity, latent heating, and latent cooling along WCB trajectories?
2. Which uncertain microphysical parameters are particularly important during different thermodynamic phases and ascent stages of the WCB airstream?
3. How spatio-temporally consistent are the key uncertainties?

Details about the case study and analysis methodology are provided in Section 2 followed by a discussion on the selection of first-order important parameters (Section 3). We then discuss the spatio-temporal consistency of parameter sensitivities in Section 5 before a detailed discussion of the first-order important parameters for different cloud and ascent regimes in Sections 4 to 6. The paper concludes with a summary and discussion of the key results (Section 7).

2. Data and methods

We analyze the cloud-microphysical parameter sensitivity evaluated using AD for a WCB ascending in the North Atlantic region in early October 2016. Fig. 1 illustrates the geographic structure of the cloud band associated with the WCB as observed from satellite and represented in our model simulations. The case study is described in detail in Oertel et al. [33]. We use trajectories provided by a high-resolution NWP framework developed for capturing atmospheric dynamics with explicit deep convection. Along those trajectories, AD is applied by resimulating the microphysical evolution given thermodynamic data, vertical velocity, and precipitation from above by pre-calculated trajectories.

2.1. ICON simulation including trajectory calculation, selection, and categorization

The WCB case study was simulated with the Icosahedral Nonhydrostatic (ICON) modeling framework [version 2.6.2.2;43]. The 66 h simulation is initialized from the ECMWF analysis at 18 UTC 03 October 2016 and run on a global R03B07 grid (approx. 13 km effective grid spacing) with a time step of 120 s. In the WCB ascent region, we include two refined two-way coupled nests employing R03B08 and

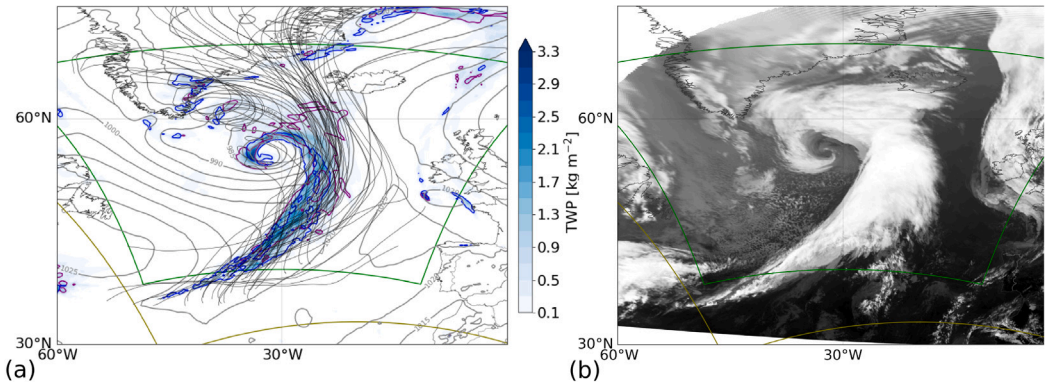

Fig. 1. Warm conveyor belt cloud band considered in this study at 18 UTC on 04th October 2016 **(a)** as modeled by ICON and **(b)** seen by Seviri 10.8 μm imager. **(a)** shows the total water path (TWP, in kg m^{-2}) in shading, the sea level pressure (every 5 hPa) in gray contours, and selected WCB trajectories starting their ascent before 18 UTC in black lines. The blue and purple contours show liquid and ice water path (at 0.5 kg m^{-2}). The greenish contours in both panels show the extent of the two inner nests.

R03B09 grids (approx. 6.5 km and 3.3 km effective grid spacing) and time steps of 60 s and 30 s, respectively. The domain set-up, along with the instantaneous total water path at 18 UTC on 04 October 2016, is shown in Fig. 1 alongside the infrared image from Seviri at the same time.

Microphysical processes are represented with ICON's two-moment scheme [41,42] which includes six prognostic hydrometeor types (cloud liquid (q_c), ice (q_i), rain (q_r), snow (q_s), graupel (q_g), and hail (q_h)), and their corresponding number concentrations. In the global domain, convection is parameterized with a Tiedtke-Bechtold scheme, while in the high-resolution nests, only shallow convection is parameterized [44–46]. ICON's default parameterization scheme for turbulence [47], subgrid scale orography drag [48] and non-orographic wave drag [49] are used. For radiative transfer, the ecRad scheme [50] is applied.

The cloud microphysics parameter sensitivity analysis focuses on the WCB, a cloud feature in extratropical cyclones highly relevant for cyclone dynamics and moisture transport to the UTLS 2. To identify the WCB, we utilize online trajectories [33,51] that are started hourly throughout the simulation on a pre-defined grid covering the inflow region of the WCB (details see Oertel et al. [33]). For subsequent analysis of microphysics parameter sensitivity with AD (see Section 2.2), the air parcel properties (longitude, latitude, pressure, air temperature, specific humidity q_v, hydrometeor content and number concentrations, as well as hydrometeor sedimentation fluxes in and out of the parcel) interpolated from the Eulerian grid to the parcel position are output every 30 s, i.e., at every timestep in the highest resolution nest.

WCB trajectory selection and ascent characteristics

From all online trajectories, we define WCB trajectories as those with ascent depth and speeds exceeding 600 hPa in 48 h consistent with other studies [33,52]. Subsequently, we focus on the period including the fastest 600 hPa ascent, as well as 2 h before the fastest ascent starts and 2 h after it ends. This also provides an ascent timescale (τ_{600}) for each trajectory [53], which varies between 1 h and 48 h. Trajectories with fast τ_{600} are influenced by embedded convection, while parcels with large τ_{600} are slowly ascending WCB trajectories. In total, about 16,000 WCB trajectories are selected by the above criteria and considered in the following analysis.

The WCB trajectories ascend in the warm sector of the extratropical cyclone, where the extended characteristic cloud band forms (Fig. 1). The cloud band has a large vertical extent spanning from the lower-most troposphere up to approximately 10 km height and includes different cloud regimes [see also33]. The extent and location of the WCB-related cloud band in our ICON simulation compare well with its position in the satellite image. Ascending WCB trajectories strongly contribute to the formation of the cloud band. They, on average, ascend from 950 hPa to 300 hPa and continuously experience colder temperatures (Fig. 2 a). Thus, from the WCB inflow in the lower troposphere to the WCB outflow in the upper troposphere, the microphysical processes shift from a predominantly warm-phase via a mixed-phase to an ice-phase. The cross-isentropic ascent of WCB airmasses is enabled by strong latent heating from cloud formation [e.g. 33] (Fig. 2 b). However, in the initial ascent phase, cloud microphysical processes can also cool the WCB parcels, for example, by rain evaporation or melting of frozen hydrometeors falling into the low-level air parcels from higher altitude clouds (Fig. 2 c).

Trajectory categorization

We stratify the trajectory data for detailed sensitivity analysis into (i) different microphysical regimes according to the dominant hydrometeors and microphysical processes and (ii) dynamical regimes in the WCB ascent. Distinctly different physics processes characterize the cloud evolution in these regimes, and we investigate whether this is reflected in different parameter sensitivities.

The *microphysical regimes* are defined by the presence/absence of certain hydrometeor types as follows: The warm-phase regime includes all trajectory segments with cloud water and/or rain but no ice-phase hydrometeors. Conversely, the ice-phase regime includes all trajectory segments, with ice-phase hydrometeors but no liquid hydrometeors. The remainder of trajectory segments with hydrometeors are classified as mixed-phase. The number of data points and average temperature in each microphysical regime are provided in Tables 1 and 2, respectively. The mixed-phase microphysical regime is most common (50.27% of all time steps), with the ice-phase regime a close second (42.28%), and the warm-phase (7.45%) regime occurring less frequently. The average temperatures are consistent with physical expectations, i.e., warm-phase processes dominate above the freezing level at 273 K, and no supercooled liquid water appears at temperatures below 233 K. Note that for technical reasons, we only use the precipitation from above, at the start and end of a resimulated time step for phase identification. In rare cases, a frozen hydrometeor such as snow may form and evaporate within a single time step without any frozen hydrometeor at the intake, start, and end of a time step. This can lead to small gradients to the corresponding parameters in cloud phases that should not be susceptible to sensitivities in the given physical processes. Key parameter sensitivities for the different microphysical regimes are discussed in Section 4.

Two different categorizations of *dynamical regimes* are used: (i) The ascent timescale τ_{600} is utilized to distinguish slowly ascending trajectories from those with significant contributions from (embedded) convection. Trajectories are grouped in τ_{600} bins of 2 h. (ii) WCB inflow, ascent, and outflow phases are separated to focus on the different dynamical forcing in these regions [54–56] To determine these, we use fixed vertical layers: Trajectory points with $p \geq 800$ hPa are classified as inflow, those with 800 hPa $> p >$ 400 hPa as ascent, and those with $p \leq 400$ hPa as outflow. The number of data points and mean temperature in each category are detailed in Tables 1 and 2, respectively. Since some trajectories reside longer in the microphysically and dynamically less active inflow or outflow regions than others, we cut off any data

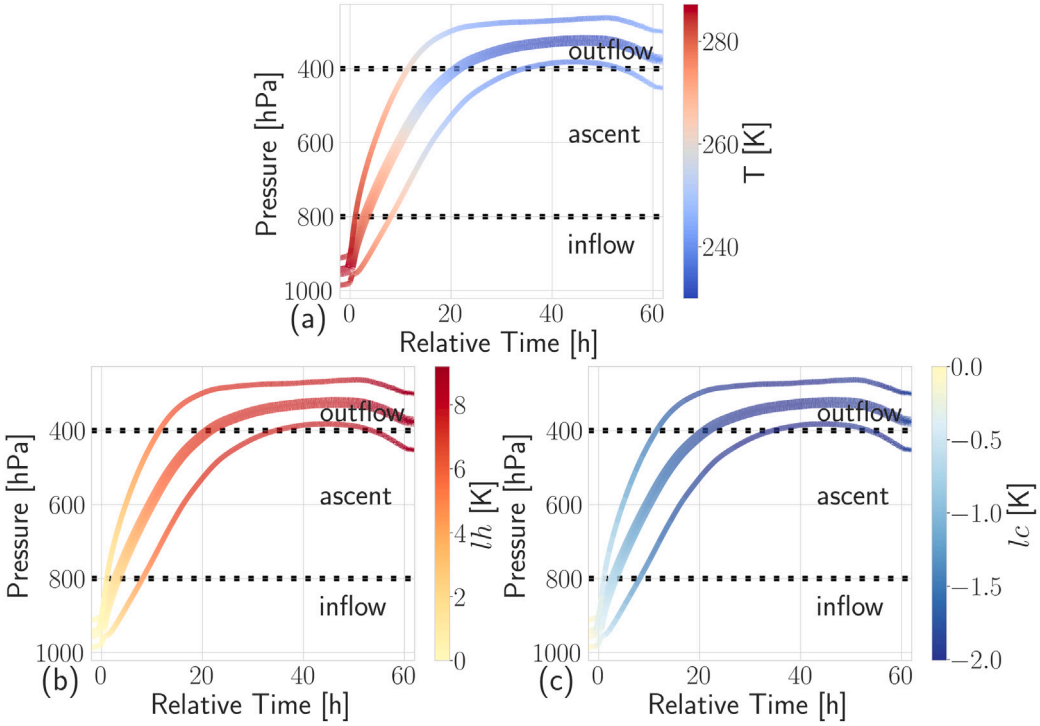

Fig. 2. Evolution of mean pressure (bold lines) and standard deviation (thin lines) along ascending WCB trajectories centered relative to the start of their fastest 600 hPa ascent phase and colored according to **(a)** mean temperature (T), **(b)** mean ascent-integrated latent heating (lh), and **(c)** mean ascent-integrated latent cooling (lc).

Table 1
Number of data points along WCB trajectories found in the different microphysical (warm-phase, mixed-phase, ice-phase) and dynamical (inflow, ascent, outflow) regimes. The percentage of all data points falling in a specific category is provided in brackets. Only data points within the strongest 600 hPa ascent and 2 h before the ascent starts and 2 h after it ends are included.

Phase	Inflow	Ascent	Outflow	Total
Warm-phase	7.07×10^6 (6.91%)	5.55×10^5 (0.54%)	0 (0.00%)	7.62×10^6 (7.45%)
Mixed-phase	1.22×10^7 (11.97%)	2.83×10^7 (27.65%)	1.09×10^7 (10.66%)	5.14×10^7 (50.27%)
Ice-phase	344 (≈0%)	4.58×10^6 (4.47%)	3.87×10^7 (37.80%)	4.33×10^7 (42.28%)
Total	1.93×10^7 (18.87%)	3.34×10^7 (32.66%)	4.96×10^7 (48.46%)	1.02×10^8 (100%)

points that are 2 h before or after their fastest 600 hPa ascent. With this modification, about a third of the WCB data points is in the ascent region (32.66%) even though the trajectories ascent very quickly. The inflow (18.87%) region occurs less often, whereas the outflow (48.46%) region dominates in our dataset. This dominance is because some trajectories ascend further after the strongest 600 hPa ascent (see, e.g., Schwenk and Miltenberger [57]). The parameter sensitivities for the different dynamical regimes are discussed in Sections 4 and 6.

2.2. Algorithmic differentiation for cloud microphysics

Algorithmic Differentiation (AD) is a technique for efficiently and semi-automatically evaluating parts of the Jacobian of an implemented model, i.e., computer code. Since any computer code is a concatenation of differentiable elemental operations, such as multiplication or trigonometric functions, one can calculate the gradient for all these operations. Applying the chain rule repeatedly gives the gradients for the whole program run alongside the usual execution of the code [15]. Since gradients can be evaluated for any prognostic variable with respect to any model parameter, a gradient above zero reveals any associated process that had been active. AD can be applied in forward mode to propagate derivatives from the inputs to the outputs and in reverse mode for, e.g., backpropagation or if many inputs, such as model parameters, and few outputs, such as prognostic variables, are in place. The gradients provided via AD are exact up to machine precision as this method does not rely on numerical differentiation.

Baumgartner et al. [58] and Hieronymus et al. [13] applied AD on cloud microphysical models to perform a sensitivity analysis. Baumgartner et al. [58] showed that AD, in principle, works for cloud schemes using idealized trajectories and a simple warm-rain microphysics scheme. Hieronymus et al. [13] extended that approach to a two-moment cloud scheme by Seifert and Beheng [41] and applied it along representative trajectories. They evaluated the gradients for 177 model parameters at low computational cost. Furthermore, they showed that instantaneous sensitivities have meaning beyond a single time step by comparing them to the ensemble spread after 30 min from a Monte-Carlo type perturbed parameter ensemble simulation. The AD-estimated sensitivities and perturbed ensemble spread ranges show a high rank correlation. This confirms that the ranking of parameter impact from AD-estimated sensitivities is consistent with parameter impact on uncertainty of cloud model simulations (at least) over a horizon of the next 30 min.

Table 2
Average temperature of WCB trajectory points found in the different microphysical (warm-phase, mixed-phase, ice-phase) and dynamical (inflow, ascent, outflow) regimes. The average temperature of all trajectory points in a specific category and the standard deviation (in brackets) are provided. Only data points within the strongest 600 hPa ascent as well as 2 h before the ascent starts and 2 h after it ends are included. The ice-phase during the inflow stems from the sedimentation of frozen hydrometeors from above that do not melt or evaporate immediately. This affects only a few trajectory data points (see Table 1).

Phase	Inflow	Ascent	Outflow	Total
Warm-phase	287.25 K (±3.49 K)	279.92 K (±2.48 K)	–	286.72 K (±3.92 K)
Mixed-phase	283.97 K (±4.00 K)	261.88 K (±11.25 K)	237.70 K (±6.57 K)	262.01 K (±17.97 K)
Ice-phase	276.15 K (±2.45 K)	246.15 K (±6.18 K)	228.29 K (±5.70 K)	230.10 K (±9.03 K)
Total	285.17 K (±4.13 K)	260.02 K (±12.33 K)	230.29 K (±8.03 K)	–

Here, we apply AD to cloud model simulations following a similar approach to Hieronymus et al. [13]. We use more trajectories to gain insight into the spatiotemporal variability of parameter sensitivity: A cloud box model is run along all WCB trajectories identified in the ICON simulation (Section 2.1). The box model consists of a reimplementation of the ICON's two-moment microphysics scheme and uses the thermodynamic time evolution from the ICON online-trajectories. The thermodynamic data and precipitation from above are provided ICON. We use temperature, pressure, ascent velocity, precipitation from above, and water content by ICON at the start of the considered trajectory segment. At every resimulated time step, we update these with input from ICON, except for water content. In addition to the cloud microphysical state, the derivatives of specific humidity (q_v), latent heating (lh), and latent cooling (lc) with respect to the model parameters are calculated to quantify the respective sensitivities. Sensitivities ζ are defined here as the (linearly) predicted change of the model state $k \in \{lh, lc, q_v\}$ if the respective model parameter p was perturbed by 10% at trajectory i, and time t:

$$\zeta^{p}_{t,i,k} = \left.\frac{\partial k}{\partial p}\right|_{t,i} \cdot 0.1p. \tag{1}$$

We multiply the 10% to the gradient to make the impact of all parameters comparable despite the different ranges of their absolute values. Without normalization, a parameter regarding the geometry of ice would be deemed much more important than a parameter related to the number of aerosols in the air due to the different units and, therefore, different nominal values. Note that different parameters may have different impacts, e.g., linear or exponential, which is taken into account at the given time t with $\partial k/\partial p|_{t,i}$.

This study considers sensitivities to 169 uncertain model parameters in the microphysics scheme and their general impact on the cloud model. For a complete list of analysis parameters and their role in the microphysics parameterization, see Hieronymus et al. [13]. The subset of parameters that we identify to be of leading order importance (as defined in Section 3) are listed and described in Tables C.4–C.8. Instead of referring to individual parameters in the following analysis, we group the identified impactful parameters according to the microphysical processes in which they appear, or if they appear in multiple processes, we group them according to the physical description. As follows for the analysis presented later, most influential parameters are directly related to the model representation of (i) diameter-mass relations of hydrometeors, (ii) rain evaporation, (iii) CCN activation, (iv) hydrometeor fall velocity. Further, parameters from the description of freezing of rain, sedimentation velocities, and the melting of frozen hydrometeors are found to be of leading order importance. Parameters that describe the geometry of a hydrometeor are examples of parameters that appear in many physical process representations. For instance, $\mathrm{geo}_{b,\mathrm{rain}}$ is used to calculate the mean diameter of a raindrop based on the rain mass and number concentrations [42]. The mean diameter, in turn, describes raindrop break-up, rain evaporation, sedimentation, riming, and freezing. A description of top parameters and the microphysical process parameterizations in which those are used is provided in Tables C.4, C.5, C.6, C.7, and C.8.

The target variables q_v, lh, and lc are selected because they are tightly related to the diabatic heating in the WCB and, therefore, have an impact on the WCB and large-scale dynamics, [e.g., 33].

3. Selecting first-order important cloud microphysical parameter sensitivities in the WCB ascent

3.1. An illustrative example

In this subsection, the thermodynamic evolution and AD output of two exemplary trajectories illustrate the variability of parameter sensitivity along the WCB ascent. We discuss the differences between a convective and a slantwise ascent and the physical plausibility of the AD-estimated sensitivities. We follow the categorization by Oertel et al. [59], who define convective WCB ascent for trajectories with ascent of 600 hPa in less than three hours and slantwise ascent for 600 hPa ascent between 6.5 h and 22 h. We further present the temporal distributions of sensitivities. The thermodynamic evolution and some AD output of the two exemplary trajectories are shown in Fig. 3. These have been selected to represent slantwise (Fig. 3 dashed lines) and embedded convection modes (Fig. 3 solid lines) and have ascent timescales τ_{600} of 41.8 h and 13.1 h, respectively. Their thermodynamic evolution is shown in panels Fig. 3 a and b and is broadly similar to the average WCB trajectory shown in Fig. 2.

As expected the strong pressure decrease (green lines in Fig. 3 a) coincides with a strong drop in temperature (dark red lines in Fig. 3 a), decline of specific humidity (blue lines in Fig. 3 b), and presence of hydrometeor content (green lines in Fig. 3 b). The phase transition of water also results in strong latent heating (dark red lines in Fig. 3 b). The target variables used in our study, i.e., specific humidity, latent heating, and latent cooling, show systematic variations as a function of air temperature in the exemplary trajectories (Fig. 3 b) as well as in all considered trajectories (Fig. 4 a and b): Specific humidity overall decreases towards colder temperatures. Latent heating reaches maximum values for temperatures around 275-280 K. It decreases strongly for colder temperatures, which is expected from the vertical velocity distribution and the temperature dependence of the saturation vapor pressure. The weak local maximum in lh around 220-230 K is related to the homogeneous freezing of any remaining cloud water. Latent cooling is mainly large at warm temperatures at or above the 273.15 K-line and reflects evaporation of hydrometeors falling into the inflow air from higher level clouds [see also e.g.33]. The secondary maximum at 273 K is related to the rapid melting of sedimenting frozen hydrometeors, while rain evaporation dominates further below. Another local maximum in lc is found at 235 K, which stems from a few data points with

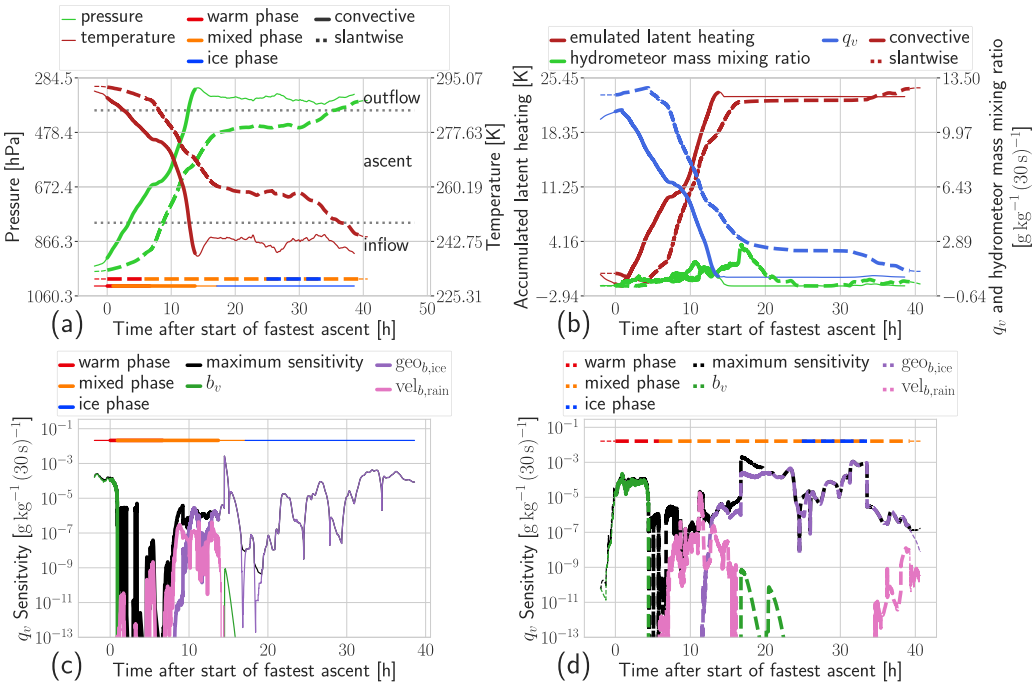

Fig. 3. Examples of convective (solid lines) and slantwise (dashed lines) ascending trajectory with τ_{600} of 13.1 h and 41.8 h, respectively. Times during the fastest 600 hPa ascent are highlighted by thicker lines. **(a)** Evolution of pressure (green, left ordinate) and air temperature (dark red, right ordinate). The horizontal lines at the bottom of the panel indicate the cloud phase as determined by our analysis (red: warm-phase, orange: mixed-phase, blue: ice-phase) for the convectively and slantwise ascending trajectories. **(b)** Evolution of accumulated latent heating and cooling $lh + lc$ (dark red, left ordinate) as well as the mass mixing ratios of water vapor (blue, right ordinate) and hydrometeors (green, right ordinate). **(c), (d)** Evolution of the maximum sensitivity (black) as determined by AD at each timestep along the convective (c) and slantwise (d) ascending trajectory. In addition, the sensitivity for three selected parameters (b_v from the parameterization of rain evaporation (green), $b_{\mathrm{geo,ice}}$ from the mass-diameter relation for ice crystals (purple), and $\mathrm{vel}_{b,\mathrm{rain}}$ from the diameter-fallspeed relation for rain (pink) are shown and sometimes cover the maximum sensitivity. Sensitivities in (c) and (d) are determined for specific humidity q_v as the target variable.

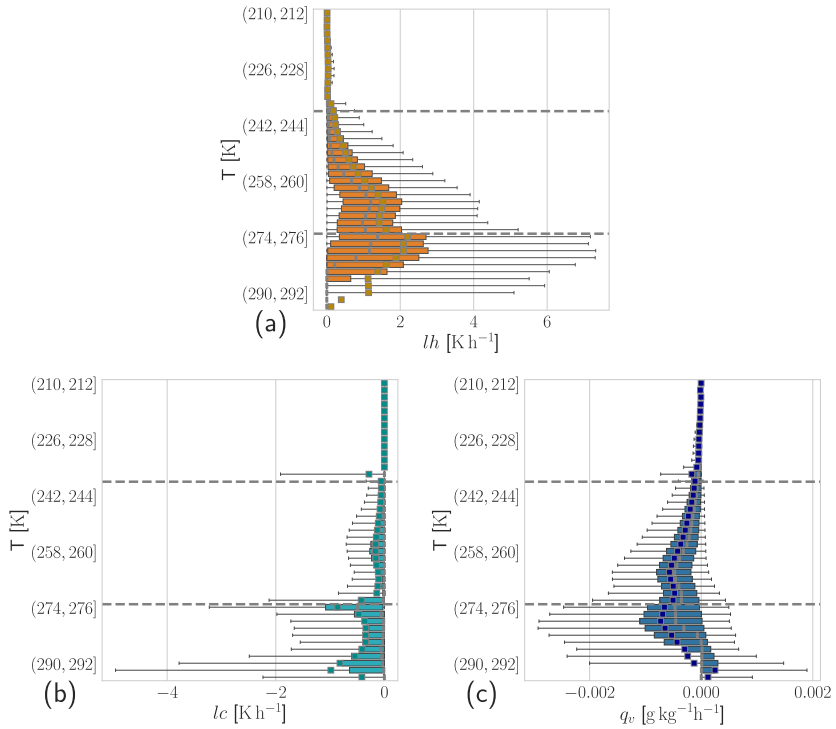

Fig. 4. Boxplots of **(a)** latent heating, **(b)** latent cooling, and **(c)** specific humidity rates along WCB ascent in 2 K temperature bins. The boxes show the median (gray) and interquartile range, and the whiskers show the 5th to 95th percentile range. Gray squares show the mean. Dashed lines mark 238.15 K and 273.15 K isotherms.

short, strong ascent and some rain present. Due to the ascent and the low temperature, the depositional growth of ice and snow is strong, which leads to a very undersaturated state with relative humidity over water as low as 65%. This triggers the evaporation of the remaining rain. However, this is a rare case that happens only in 131 of 16534 trajectories.

Fig. 3 c, d explores the uncertainty of specific humidity evolution as quantified with AD-derived sensitivities $\zeta^{p}_{t,i,k}$ (Eq. (1)) for the convective and slantwise ascending trajectories, respectively. We focus here on the sensitivity of the specific humidity q_v only. Figs. 3 c and d show the maximum sensitivity of all 169 parameters for each timestep, i.e., 30 s, along the relevant trajectory segments (black line). The maximum sensitivity along both trajectories fluctuates over a large range of values with peak values reaching 10^{-2} g kg^{-1} (30 s)$^{-1}$. There is no noticeable trend of sensitivity with temperature, specific humidity, or other physical parameters. Also, the values are comparable between the trajectories and, more generally, across different ascent timescales (not shown).

In addition to the maximum sensitivity, we show the sensitivity of q_v to three selected parameters $\mathrm{b_v}$, $\mathrm{vel}_{b,\mathrm{rain}}$, and $\mathrm{geo}_{b,\mathrm{ice}}$, i.e., the direct AD output, by the colored lines (green, pink, purple lines in Fig. 3 c,d). As expected, these parameters show a stronger dependence on time during ascent, temperature, and other physical properties of the parcel under investigation. b_v (green lines in Fig. 3 c,d) is a parameter that appears in the rain evaporation [42]. Rain evaporation describes the water flux from rain to the gas phase, and therefore, modifications to this parameterization directly impact the specific humidity $\mathrm{q_v}$. The parameter is primarily important at the start of WCB ascent when trajectories are still undersaturated and rain falls into the parcels from above. For the slantwise ascending parcel, there is a second interval of significant b_v-related uncertainty around 10 h and 25 h into the ascent, coinciding with a slight pressure increase interval. Due to the negative vertical velocity, the air parcel becomes undersaturated, and rain left in the parcel or falling in from above will evaporate (also reflected by slightly decreasing accumulated $lh + lc$).

The second parameter $\mathrm{vel}_{b,\mathrm{rain}}$ appears in the diameter-fallspeed relation of rain and appears in the parameterizations of rain sedimentation as well as the riming growth of frozen particles upon collision with rain. Sensitivity to $\mathrm{vel}_{b,\mathrm{rain}}$ is found again at the beginning of the ascent with several maxima at later times, in particular for the slantwise ascending trajectory. It only appears during periods labeled as mixed-phase. The decrease in sensitivity after the first few hours into the ascent is likely due to the depletion of rain by sedimentation, freezing, and riming. Later maxima are tied to re-introduced rain likely related to sedimentation from embedded convection above the considered parcel. However, this is not easy to demonstrate with the Lagrangian data. $\mathrm{vel}_{b,\mathrm{rain}}$. Note that the AD-derived sensitivities indicate an "immediate" impact, i.e., within one timestep, onto the target variable and disregard longer-timescale feedback processes. In the below-cloud region, altered rain sedimentation can impact rain evaporation and, thereby, specific humidity. In the presence of cloud liquid, a saturation adjustment scheme controls the partitioning between cloud water and water vapor. Therefore, the sensitivity to $\mathrm{vel}_{b,\mathrm{rain}}$ in the mixed-phase, in-cloud regions is not related to rain sedimentation but to the representation of riming growth. Riming results in additional latent heating from the freezing, impacting the parcel's temperature and, therefore, the saturation of specific humidity used in the saturation adjustment.

Eventhough $\mathrm{vel}_{b,\mathrm{rain}}$ and b_v are both related to rain, they are dominant at different stages. The early stage of a cloud is dominated by condensation and latent heat release, i.e., processes related to phase changes such as rain evaporation. The fallspeed of rain is not yet the limiting factor in determining specific humidity in the two trajectories shown in Fig. 3. Therefore, $\mathrm{vel}_{b,\mathrm{rain}}$ becomes more relevant once the cloud is developed further.

Sensitivity to $\mathrm{geo}_{b,\mathrm{ice}}$ is found across mixed- and ice-phase regions along both trajectories. $\mathrm{geo}_{b,\mathrm{ice}}$ appears in various parameterizations, including ice sedimentation, depositional growth, and riming growth. In particular, the latter two processes impact the latent heating in the mixed-phase and, by that, the parcel temperature and saturation of specific humidity. In the ice-phase, partitioning between ice particles and specific humidity is controlled by depositional growth, and, therefore, any modification of depositional growth directly impacts specific humidity.

As evident from the time dependence of the individual parameter sensitivities in the exemplary trajectories, the cloud phase influences the dominant parameter sensitivities due to different active microphysical processes, which is well expected from basic cloud physical understanding. A cloud-phase dependence of the parameter sensitivities is also reflected across all considered WCB parcels. Another important aspect of the exemplary time series of parameter sensitivities is the temporal consistency of the impact of individual parameters (Fig. 3 c, d): The segments of large parameter sensitivity are not an isolated occurrence in time but can extend over several hours. We hypothesize that the time the microphysical evolution is sensitive to a specific parameter is important. Complex, non-linear microphysical processes likely buffer short bursts of parameter sensitivity. These aspects will become important in objectively selecting leading order parameters as discussed in the following Section 3.2.

3.2. Selecting most impactful parameters

Several different approaches can be used to identify parameters with a large impact across various trajectories and over a large region. It is critical to understand the spatio-temporal variability of parameter sensitivity to retain variability inherent in the strong dependence of active cloud microphysical pathways on the local conditions. In the following, we introduce a method derived from first principles to quantify sensitivities gathered by the approach presented in Section 2.2.

Instantaneous ranking of sensitivities

An intuitive way is to gather parameters with sensitivities ζ in the leading order of magnitude for each target variable, i.e., latent heating rates (lh), latent cooling rates (lc), and specific humidity (q_v), at each time step during the fastest 600 hPa ascent. This approach retains much of the temporal and spatial (in the sense of different trajectories) variability of parameter sensitivities, at least in a relative sense. Due to the temporal evolution of thermodynamic conditions and updraft velocity, sensitivity to specific parameters may only exist during certain time periods before and after which they cease to be important. Information on the length of timespans τ_{min}, during which a specific parameter is coherently within the leading order, may be important for selecting important parameters. This argument is based on the hypothesis that the time the microphysical evolution is sensitive to a specific parameter is important and that sensitivities registered only over a short time or very localized spatial extend may be less important due to the strongly non-linear nature of cloud physics. Finding a suitable choice for a "significant" τ_{min} is not trivial. An intuitive approach may be normalizing it with the time a parcel spends within the cloud or a specific cloud phase, which is roughly proportional to the ascent time τ_{600}. Using a threshold of $\tau_{min} = 1\%\tau_{600}$ and retaining only parameters that appear in at least 0.1% of all trajectories yields 74 parameters in our WCB dataset (see Section 6 for more details). This parameter number is too large to be fully targeted by full NWP ensemble simulations, and therefore, either the percentage of time needs to be increased or additional criteria need to be applied, such as information on the absolute sensitivity values and/or combinations of target variables. An issue with the former is that processes with a short inherent timescale, such as CCN activation or homogeneous cloud freezing, may be disregarded, although they may have a lasting impact on cloud microphysical evolution. Furthermore, using the leading order of magnitude in each time step removes opportunities to compare time steps other than analyzing ranked lists of parameters. Aside from

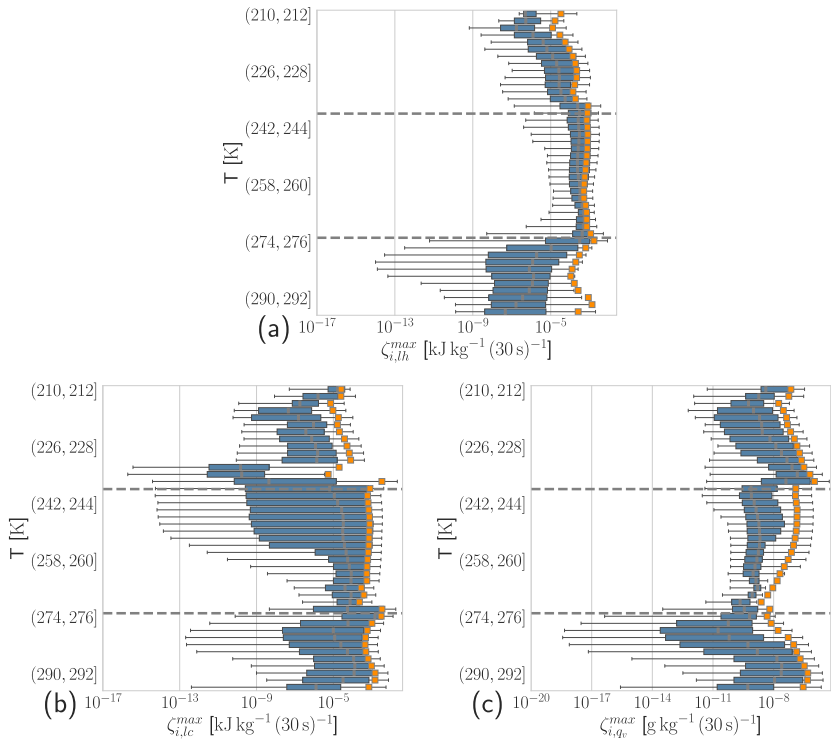

Fig. 5. Boxplots of maximum sensitivities per time step of **(a)** latent heating and **(b)** cooling rates, and **(c)** specific humidity changes along WCB ascent in 2 K temperature bins. The boxes show the median (gray) and interquartile range, and the whiskers show the 5th to 95th percentile range. Gray squares show the mean. Dashed lines mark 238.15 K and 273.15 K isotherms.

comparing the identified parameters with other approaches later in this section, we, therefore, do not use this approach.

At last, this approach does not necessarily include the inflow (p≥ 800 hPa) and outflow (p≤400 hPa) of the trajectories when the fastest 600 hPa ascent starts above the typical inflow area or ends below the outflow area. Including additional time steps before the ascent starts or after it ends may resolve this issue but introduce a more severe one. These periods can contain minimal activity, resulting in spurious data points where derivatives are near zero. Consequently, parameter rankings within these time steps lack meaningful interpretation, as they are based on negligible changes.

Ranking sensitivities based on single trajectory maximum (method used in further analysis)

The instantaneous approach discussed previously disregards information on the absolute values of parameter sensitivities and is thereby impacted by segments with overall low sensitivity. This dependence on the local conditions is reflected by the systematic variations of absolute parameter sensitivities with ascent timescale, e.g., temperature and, thereby, cloud phase. Fig. 5 shows the distribution of the maximum parameter sensitivity per time-step as a function of parcel temperature (for all trajectories). Similar to the value of the target variables (Fig. 4 a,b), there are systematic changes at temperatures of 273.15 K and 238.15 K, i.e., where phase changes are expected. The parameter sensitivity of specific humidity, for example, is particularly large at warm temperatures below the cloud base, where rain evaporation occurs, and at temperatures just below the homogeneous freezing temperature. Conversely, the sensitivities are particularly large for latent heating in the mixed-phase temperature region. This presumable reflects the impact of glaciation: While ice formation via freezing of ice in the mixed-phase regime modifies latent heating, the specific humidity is tightly controlled by water saturation over liquid as long as cloud liquid is present. To reflect the variation of sensitivities with cloud phases, we introduce another approach that retains variability across cloud phases and trajectories but minimizes the impact of segments with low sensitivity.

For each cloud phase j and each trajectory i a maximum sensitivity $\zeta^{max}_{j,i,k}$ for target $k \in \{q_v, lh, lc\}$ is determined:

$$\zeta^{max}_{j,i,k} = max_{p,t^\star}\left(|\zeta^{p}_{t^\star,i,k}|\right) \quad \text{with } t^\star = (t \mid \text{phase} = j),\ j \in \{\text{warm}, \text{mixed}, \text{ice}\}. \tag{2}$$

Based on this maximum sensitivity parameters with leading order impact $\chi^{p}_{t,i,k}$ are be selected according to:

$$\chi^{p}_{t,i,k} = \left(|\zeta^{p}_{t,i,k}| \geq 0.1 \cdot \zeta^{max}_{j,i,k}\right) \tag{3}$$

Relying solely on Eq. (3) criterion, where a parameter yields $\chi^{p}_{t,i,k} = 1$, is sensitive to outliers and yields many parameters since a list of parameters for any trajectory i would be compiled. We calculate the fraction of data points where $\chi^{p}_{t,i,k} = 1$ and use this to create a criterion:

$$P(\chi^{p}_{k} > 0|j) = \sum_{i}\sum_{t^\star}\frac{\chi^{p}_{t^\star,i,k}}{n^\star} \quad \text{with } t^\star = (t \mid \text{phase} = j),\ j \in \{\text{warm}, \text{mixed}, \text{ice}\}, \tag{4}$$

where $n^\star$ is the total number of data points for a given phase. A parameter p is then considered important for a target k at phase j if following holds: The criterion is then:

$$P(\chi^{p}_{k} > 0|j) > 0.1\% \quad \text{for any } k \in \{q_v, lc, lh\},\ j \in \{\text{warm, mixed, ice}\} \tag{5}$$

This way, only parameters with non-zero impact $\chi^{p}_{t^\star,i,k}$ in at least 0.1% of all data points given a cloud phase j and target variable k are retained. This approach generates a list of 38 important parameters (see Table C.3), which, although still potentially too extensive for practical use in full NWP ensemble simulations or even real-time parameter selection during simulations, represents a substantial reduction in the number of parameters compared to the previously discussed approach.

We deem this method to be robust and adequate for further analysis in this paper because of the following reasons:

- All parameters deemed important in previous single to few parameter sensitivity studies are identified [e.g. 9,12,35,37–39].
- Identified parameters for different timescales vary, reflecting previously documented differences in microphysical pathways [e.g. 33,52,57].
- Identified parameters vary with cloud phase consistent with a basic understanding of cloud microphysical pathways and process dependencies.
- Parameters have a large impact, i.e., are within the leading order of magnitude, and segments with very low parameter sensitivity are ignored.
- Parameters with a very short-lived impact are ignored due to the criterium on the minimum number of data points (Eq. (5)).

However, note that a disadvantage of this method is that it is not useful for an online determination of key parameters during an NWP simulation as it requires information of extended trajectory segments and hence is only applicable to postprocessing of simulation data.

The thresholds within a trajectory from Eq. (4) and over all data points in Eq. (5) can be changed according to the requirements. For example, the threshold within a trajectory can be increased to reduce the number of selected parameters, or the threshold over all data points can be increased to gather a list of parameters with a more generalizable impact.

Comparison with previously published approaches

In previous work, Hieronymus et al. [13] used the mean squared sensitivity over all trajectories i (with n_{traj} the number of trajectories) and timesteps t (with n_{time} the number of time steps) for each parameter p a given k:

$$\overline{\zeta_k^p} = \frac{1}{n_{\text{time}} \cdot n_{\text{traj}}} \sum_{i}^{n_{\text{traj}}} \sum_{t}^{n_{\text{time}}} (\zeta_{t,i,k}^p) \tag{6}$$

Then, the ten parameters with the highest average for each target k are examined in detail in their approach. This method ignores systematic variability of absolute parameter sensitivity across different cloud phases and vertical velocity regimes. This may be particularly problematic if certain regimes' impact on the targeted flow/cloud system structures is not proportional to their occurrence frequency in the dataset. When using the square root of Eq. (6) to maintain the same units as in our approach and select all parameters within the highest magnitude, then the method yields 15 parameters in this case study (see Table C.3). This approach can be partially improved by defining a maximum mean squared sensitivity for different cloud phases, resulting in a large set of identified parameters (see Table C.3). However, using the mean gives parameters with a consistent but low impact the same rank as those with a shorter but very large impact. In the context of microphysical models, the latter is of special interest as this indicates an environment where slight changes in the model parameter lead to significant changes in the simulation. Therefore, and because variability with vertical velocity regime is absent, we do not use this approach in the following analysis.

The different methods are compared in Fig. 6, where the original method by Hieronymus et al. [13] captures the least number of parameters. While introducing phases yields parameters related to CCN activation, it does not capture some parameters for Hallet–Mossop ice multiplication and those relevant during the inflow, i.e., rain sedimentation and evaporation parameters. Our method yields these parameters but leaves out outliers, such as parameters relevant to hail size, which are given by the intuitive approach with minimum timespans τ_{min}. Due to mostly moderate vertical velocities in WCBs, hail hardly occurs, and even only few hail particles are mostly unexpected. However, the minuscule amounts of hail present in the trajectory data lead to outliers in the sensitivities. For example, if small amounts of hail fall to lower layers of the atmosphere, they rapidly evaporate entirely, i.e., faster than the time step of our simulation. Such instantaneous processes lead to exploding gradients when calculating the derivative of specific humidity to any associated parameter. Changing the parameter, i.e., expediting or slowing the process, has no impact because either the process is already handled within one time step or it had to be slowed down considerably to be broken up into at least two time steps. Without much more hail that can evaporate in this layer or below, the transfer of water and latent heat release is limited by the total amount of hail. Considering this reasoning and the fact that our approach does not produce hail parameters, this further supports the robustness of our method compared to more intuitive approaches.

Overall, it is encouraging that the first roughly 30 parameters are identified irrespective of the selection approach, further corroborating their importance in terms of large (at least) local impact.

4. Variation of most important parameters with cloud phase

The cloud phase, i.e., the cloud composition in terms of the phase state of water, determines which microphysical processes are active and, thus, influences specific humidity q_v, latent heating lh, and latent cooling lc, as well as associated maximum sensitivities (Fig. 4). Consistent with this expectation, warm-, mixed-, and ice-phase cloud segments are sensitive to different parameters (Fig. 7 a). Table C.9 lists the identified leading-order parameters for each target variable and cloud phase. Note that the leading-order parameters between the warm- and ice-phase segments do not overlap (except for dynamic viscosity of air $\nu_{kin,air}$), while there is a significant overlap of parameters selected in the mixed-phase cloud segments with either warm- or ice-phase cloud segments. This is plausible, as physical processes in warm- and ice-phase clouds are very different, while processes from warm- and ice-phase regimes are also expected to be important in mixed-phase clouds. Overall, the magnitudes of the mean sensitivities for q_v, lh, and lc are largest for the mixed-phase and smaller for the ice- and warm-phase (Fig. 7 a).

Notably, the impact of geometry-related parameters is very pronounced at all cloud stages. Since we use bulk microphysics, the average size of a hydrometeor is estimated using these geometry parameters. As a result, this parameterization is widely applied in various processes where the size of hydrometeors is essential, such as evaporation, melting, collision, and sedimentation. The ubiquitous appearance is illustrated in Figs. 8–10 where geometry plays a crucial role at all stages of a cloud. Consequently, a comprehensive discussion of these parameters becomes impractical.

In the following, we detail the important parameters for each cloud phase.

4.1. Warm-phase cloud segments

In Fig. 8, we show the processes and parameterizations associated with leading-order parameters during the warm-phase cloud segments. The largest sensitivities in warm-phase clouds are related to rain evaporation, diameter-size relation of rain (which also influences rain evaporation), and CCN activation (Fig. 7 a and Table C.9). Parameters used to represent rain evaporation and the rain size distribution impact only q_v and lc, as rain evaporation is associated with replenishing q_v and evaporative cooling. Rain evaporation is important at the beginning of the WCB ascent when rain from higher-level clouds reaches low-level, still undersaturated parcels. In contrast, although with a much smaller mean impact, parameters in the CCN activation parameterization influence lc, q_v, and lh. The small sensitivity to CCN activation arises due to additional water mass transfer and associated heating of the parcel during CCN activation.

Overall, rain evaporation and CCN activation dominate parameter sensitivities in all three target variables in the warm-phase cloud segments. However, sensitivities to CCN activation are rather small, and lh parameter sensitivity overall is much lower than in the mixed-phase cloud segments. Also note that if a model with a prognostic

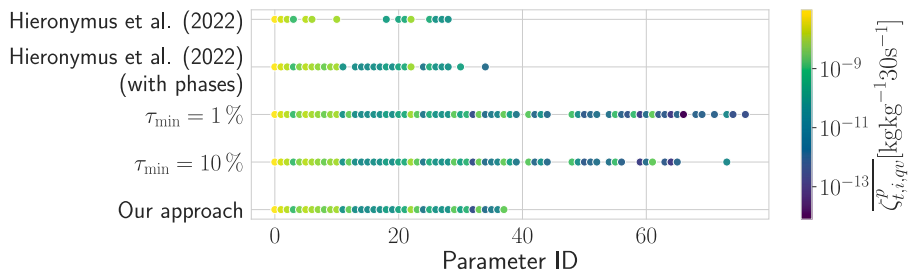

Fig. 6. A comparison of the parameters deemed important by different approaches. The parameters are sorted by the importance given by our approach defined in Eq. (4). Parameters 80 to 169 are not shown but also not selected as important by any of the methods. The colors represent the average sensitivity for q_v over all trajectories and time steps.

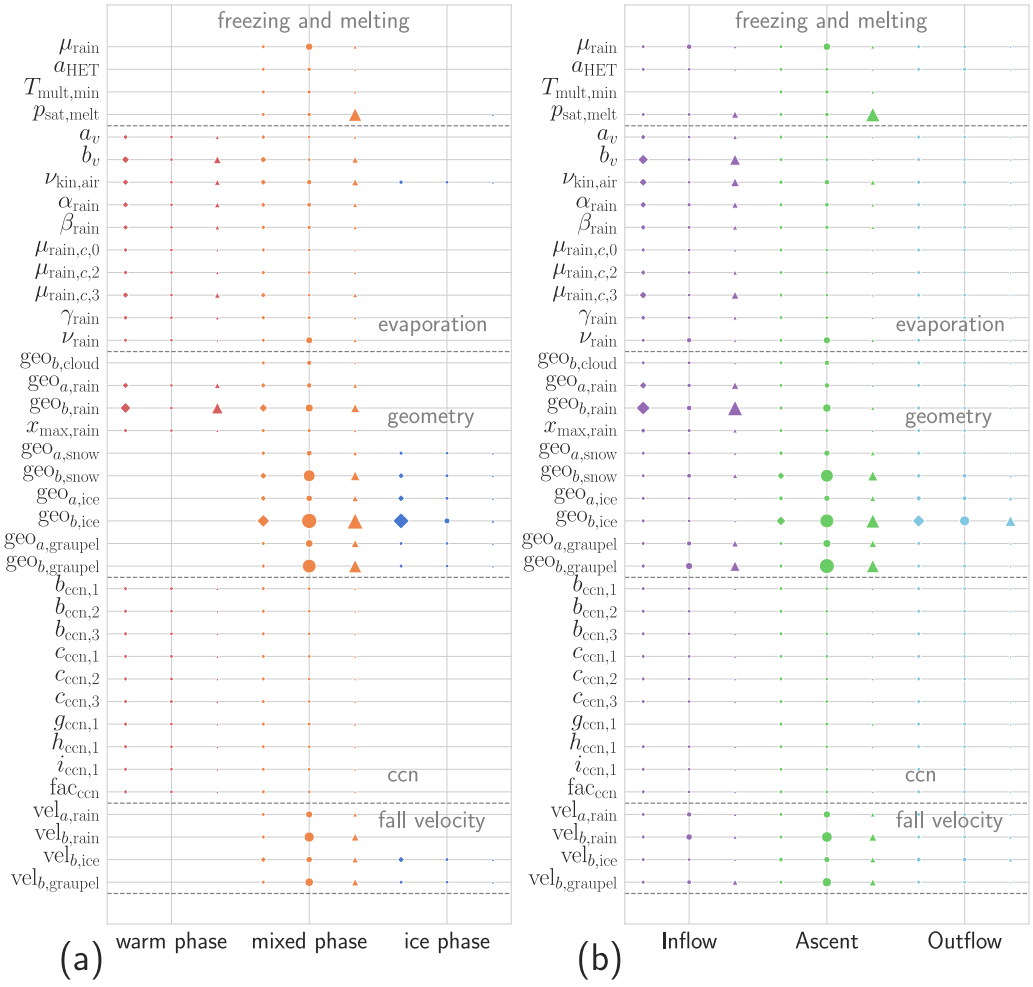

Fig. 7. Mean gradients $\overline{|\zeta^{p}_{r*,i,k}|}$ for $k \in \{q_v, lh, lc\}$ (diamond, circle, triangle) stratified in **(a)** the warm, mixed, and ice-phase and **(b)** inflow, ascent, outflow along WCB trajectories. The size of the markers is proportional to the mean gradients for each target. The scaling for q_v is higher than for lh and lc as gradients for q_v are smaller.

condensation (and not a supersaturation scheme) is used, more considerable sensitivity to parameters in the condensation description and CCN activation are expected.

4.2. Mixed-phase cloud segments

In mixed-phase cloud segments, the largest number of leading order parameters is found, as expected from the complex cloud composition and corresponding multitude of active processes (Figs. 7a and 9, Table C.9). Most parameters relevant in the mixed-phase cloud segment have also been identified as important in either warm- or ice-phase cloud segments. q_v is most strongly influenced by parameters used to describe the geometry of ice and snow particles and, to a lesser degree, those used in the rain evaporation parameterization (Fig. 7 a). Generally, q_v is sensitive to all identified leading order parameters. lc displays similar sensitivities as q_v with additional contributions from parameters describing graupel geometry, diameter-fallspeed relations, and melting. The impact of rain evaporation again likely arises from subsaturated parcels at the beginning of the ascent in regions where there is sedimentation of frozen particles (graupel, snow) from clouds at higher altitudes. This also explains the impact of parameters in the fallspeed-diameter relationship, graupel geometry, and melting parameterization. Melting influences lc through its direct cooling effect, affecting the local temperature and humidity. This process competes

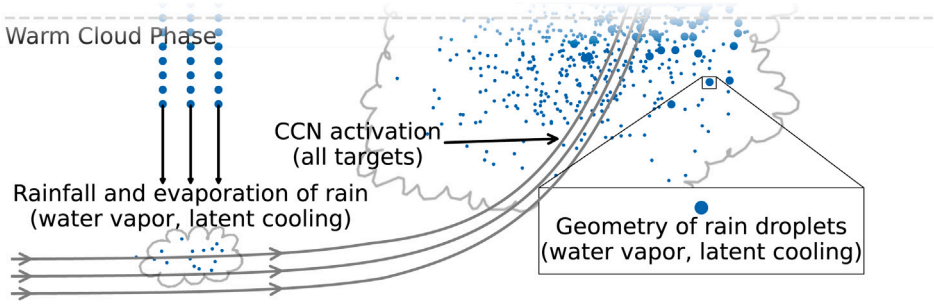

Fig. 8. An overview of active processes and parameterizations with important parameters involved during the warm-phase. Small blue dots represent cloud droplets, and large dots represent raindrops. The gray lines indicate the direction of the WCB trajectory.

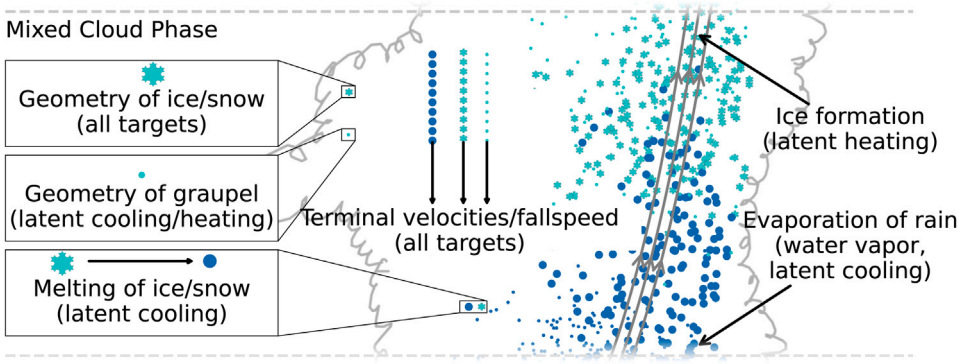

Fig. 9. An overview of active processes and parameterizations with important parameters involved during the mixed-phase. Small blue dots represent cloud droplets, and large dots represent raindrops. Dots in cyan represent graupel, whereas snowflakes represent ice and snow. The gray lines indicate the direction of the trajectory.

with sublimation and deposition in determining the availability of frozen hydrometeors in unsaturated air parcels. Furthermore, melting alters frozen hydrometeors' size distribution and density, modifying their sedimentation rates. These effects contribute to the sensitivity of lc to parameters controlling graupel geometry, diameter-fallspeed relations, and melting. In addition, rain evaporation can occur in conditions favorable for the Wegener–Bergeron–Findeisen process, as the rain evaporation parameterization is called in between the vapor deposition parameterization and the second saturation adjustment. Hence, we may see subsaturation to liquid due to ice deposition. lh is most strongly influenced by parameters describing ice, snow, and graupel geometry, followed by parameters used to describe particle sedimentation and ice formation, i.e., the freezing of rain. These parameters play a role in cloud glaciation and, therefore, control latent heat released from vapor deposition, freezing, and riming. As latent heating impacts the parcel temperature, instantaneous impacts on q_v are expected to occur as well, although q_v in the mixed-phase is directly controlled only by the saturation adjustment scheme. Terminal velocities play a role in depositional growth (ventilation) and riming and, therefore, impact lh (and q_v) by a similar mechanism. However, fall velocity for rain and graupel are not identified as leading order parameters for q_v but only for lc, likely the indirect impact on q_v via altered temperatures is too small and too localized.

Overall, the mixed-phase cloud region is characterized by the largest sensitivities and the most parameters within the leading order of magnitude, dominated by rainfall parameterization and geometry for ice, snow, and graupel.

4.3. Ice-phase cloud segments

In ice-phase cloud segments, the leading-order parameter sensitivities are related to the diameter-mass relation of ice and its fall velocity (Figs. 7 a and 10, Table C.9). The sensitivities are similar for all three investigated target variables. Smaller sensitivities, which are still leading order, are also found for parameters related to the diameter-mass relation and fall velocity of snow and graupel. This reflects the presence of pure ice-phase clouds, mainly in the outflow region of the WCB. Ice crystals are the predominant particle type found in these clouds, with some snow and graupel that are carried in the stronger updrafts and will quickly sediment. As vertical velocities and net vertical displacement in the outflow are typically relatively small, the main active cloud microphysical process is the sedimentation of ice crystals.

5. Spatio-temporal consistency of parameter sensitivities

To analyze spatial and temporal patterns of sensitivities, we transform the Lagrangian sensitivity information onto an Eulerian grid. At each position of the 4D Eulerian grid, we store the frequency of each parameter where the parameter is within the leading order of magnitude as defined in Eq. (3) for a given target k. That is, each position contains $\sum_{\hat{\imath},i} \chi^p_{\hat{\imath},i,k}$, with $\hat{\imath}$ the time where trajectory i is within the corresponding bin. The new four-dimensional grid covers the area of the WCB ascent, i.e., 17 to 84.32 °N and −68 to 68.62 °E with 100 equidistant bins along the longitude and latitude with a constant increment in longitude and latitude values, the entire atmospheric column (10 height levels from 0 hPa to 1000 hPa with a spacing of 100 hPa) and the entire duration of the original model simulation, i.e. 0-72 h in 1 h interval. We use 2 h before the ascent starts, the fastest 600 hPa ascent, and 2 h after the ascent ends of each trajectory. This metric depends on how many trajectories pass through a bin and how fast each one leaves it again.

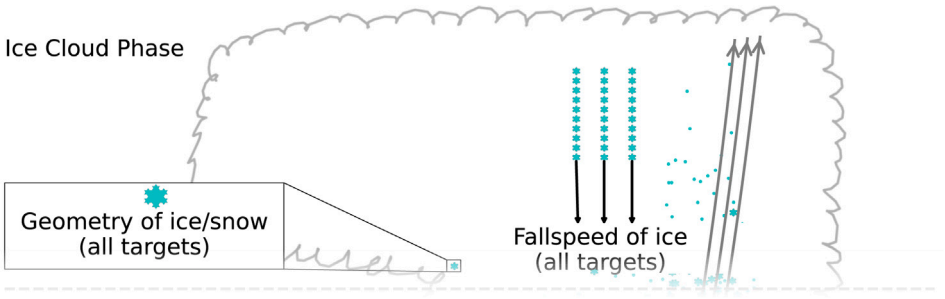

Fig. 10. An overview of active processes and parameterizations with important parameters involved during the ice-phase. Dots in cyan represent graupel, whereas snowflakes represent ice and snow. The gray lines indicate the direction of the trajectory.

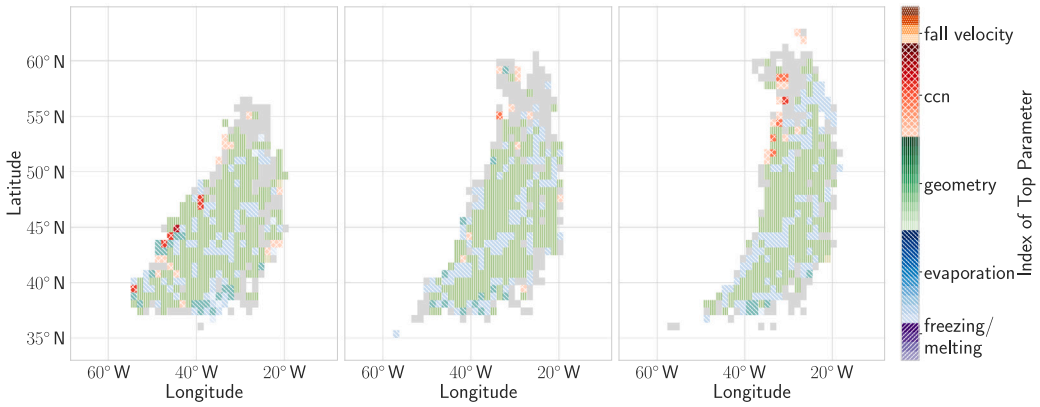

Fig. 11. The top parameters for specific humidity at 900 hPa $\leq p <$ 1000 hPa, between 1 h $\leq t <$ 2 h, 7 h $\leq t <$ 8 h, and between 13 h $\leq t <$ 14 h (from left to right) after the first trajectory started its ascent. Cells are colored according to the parameter that most frequently occurs within the leading order of magnitude in the given bin, where the magnitude is calculated for each trajectory. The gray outline shows the total area covered by our simulation within these time periods.

5.1. Spatio-temporal consistency of important parameters for specific humidity

The spatio-temporal distribution of leading order parameters in the inflow region (900 hPa $\leq p <$ 1000 hPa) is shown in Fig. 11, which displays at each grid location the most frequently found leading order parameter for q_v. The three panels show the temporal evolution of the inflow region parameter sensitivities from 1 h after the first trajectory started its ascent in 6 h steps. The general shape and evolution of the region, where parameter sensitivities are identified, reflects the shape and position of the WCB inflow region by definition. In all three time instances, geometry-related parameters for rain are most often identified, and sensitivity to these parameters occurs consistently over a large area and a large timespan. Other leading-order parameters relate to the evaporation of rain and CCN activation, although they occur less widely. Sensitivity to evaporation-related parameters seems to occur in band-like structures, and we speculate that this may be related to a strong influx of hydrometeors from banded convection at higher altitudes, which is ubiquitous in the analyzed WCB [33].

At higher altitudes, the area over which significant parameter sensitivities are identified gets smaller, up to about 600 hPa consistent with the general geometry of the WCB airstream (see Video 2d_qv.mp4). In this altitude range, CCN activation becomes the most dominant parameter sensitivity. At altitudes around 500 hPa, some areas with strong updraft are dominated by freezing. Otherwise, parameters related to freezing and melting are less frequent within the leading order of magnitude than other parameters. This becomes apparent when comparing the frequency distribution of such patches between different parameters in Fig. 12. Coherent patches with leading order sensitivities for freezing and melting are magnitudes smaller and shorter-lived than most parameters. This, however, is in line with our previous findings in Section 4. At even higher altitudes up to outflow regions (200 hPa $\leq p <$ 600 hPa), the area covered by the WCB airstream becomes larger again. Parameters related to the geometry of graupel, snow, and ice dominate, with ice the only dominating factor at 200 hPa and higher altitudes. This contrasts sensitivities at $p \geq$ 800 hPa, where the geometry of rain, snow, and graupel is dominant but not ice. Note that geometry-related parameters are used in many process descriptions, from evaporation to fall velocity and freezing and melting, which may explain the widespread sensitivity to these parameters.

For a more quantitative perspective on spatio-temporal consistency in parameter sensitivity, we identify coherent patches in space and time where one particular parameter is of leading-order magnitude. Note that this includes all parameters identified as leading-order in all locations, not just the most frequently occurring as in Fig. 11. These patches of coherent parameter sensitivity are then characterized by their maximal temporal extent and their geometric size in terms of the number of grid points (including horizontal and vertical extend). The frequency distributions of these metrics of spatial and temporal coherency are shown in Fig. 12 a and b for each parameter individually (ordinate, parameters include those identified in Section 3.2). In general, spatial and temporal consistency seem to be related, where parameter sensitivities that occur over large spatial regions also last longer than those occurring only in smaller spatial regions. This is confirmed by the correlation between spatial and temporal extend shown in Fig. 12 c.

The spatial and temporal extent of geometry-related parameter sensitivity is the largest, which aligns with our findings from above. In addition, sensitivity to evaporation- and CCN activation-related parameters is found over larger areas and time spans that cover most of the WCB ascent region. However, The spatio-temporal extent of CCN-related parameter sensitivity is smaller than those of geometry- and evaporation-related parameter sensitivity. This can be explained by the

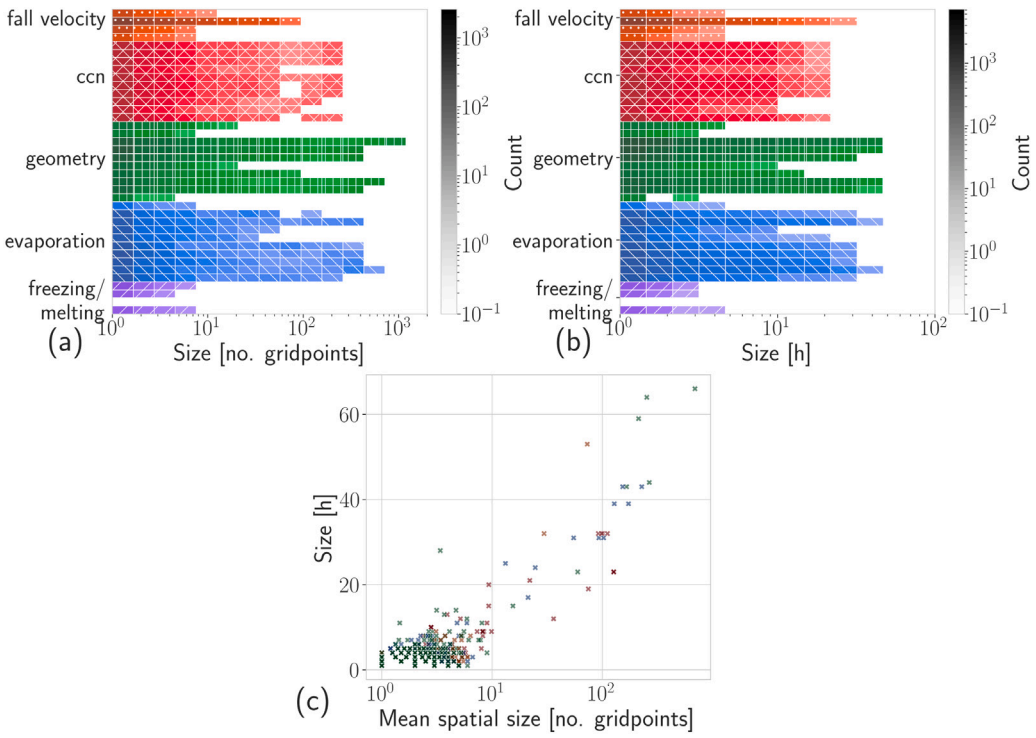

Fig. 12. Frequency distribution of spatio-temporal dimension of coherent regions with non-zero sensitivity for q_v: **(a)** spatial extend in the number of gridpoints (regridded data), **(b)** temporal extend in hours, **(c)** correlation of object spatial and temporal extend.

geometry of the WCB airstream, which is rather narrow in the lower half of the active ascent (800 hPa to 600 hPa), where CCN activation is active and spreads out more horizontally in the inflow and outflow regions, where there is no CCN activation but evaporation (mainly inflow), hydrometeor sedimentation and growths. Parameters relating to the representation of fall velocity are also found in leading order, and in particular, those related to the ice fall velocity are also found over very large spatio-temporal patches. Ice sedimentation is particularly important for the cloud evolution in the WCB outflow [e.g. 57], and it is here that we find a strong impact of parameters related to the fall velocity. Patches of coherent sensitivity to freezing- and melting-related parameters are the smallest. However, the patch sizes still extend to 3 h and several degrees in longitude/latitude. This may not be surprising as these processes do not directly influence the specific humidity aside from a small temperature change affecting the saturation pressure.

In summary, geometry-related parameters have the largest and most consistent impact on specific humidity, followed by parameters related to CCN activation and evaporation of frozen hydrometeors.

5.2. Spatio-temporal consistency of important parameters for latent heating

The spatio-temporal distribution of the most frequently found leading order parameters for lh is overall similar to that for q_v (see Video supplement 2d_latent_heat.mp4 [60]). However, there are also some major differences, particularly in that parameters related to CCN activation, fall velocity, and freezing more frequently appear as the leading order parameters. This is physically plausible, as these parameters may not much impact the partitioning between specific humidity and cloud condensate (while saturation adjustment is used in the model), but impact the glaciation state and, thereby, additional latent heat release. Freezing-related parameter sensitivity appears mainly at altitudes between 700 hPa and 300 hPa, but is the most frequently encountered parameter only in relatively small patches.

The distribution of spatio-temporal extent of coherent patches supports these findings (Fig. B.16: the largest differences to the metrics for q_v are (i) the smaller extent of regions with evaporation-related parameter sensitivity and (ii) the larger extent of regions with freezing (and melting) related parameter sensitivity. In addition, other parameter sensitivities extend over larger coherent patches (fall velocity, CCN activation, and geometry-related). The temporal extent of CCN activation is very large, which indicates a large impact of CCN activation overall on the heating budget, even if CCN activation is reduced in higher altitudes. The correlation between spatial and temporal size for lh is higher for a spatial extent larger than ten gridpoints than for q_v because the impact of CCN activation remains active over a longer time (see Fig. B.16).

5.3. Spatio-temporal consistency of important parameters for latent cooling

Also, the spatio-temporal distribution of leading order parameters for lc is similar to that for q_v (see Video 2d_latent_cool.mp4). The largest difference is an extended region with melting-related parameter sensitivity at altitudes between 900 hPa and 600 hPa. With increasing altitudes, this region expands in a southerly direction, reflecting the general temperature structure of the atmosphere.

The distribution of spatio-temporal extent of coherent patches reflects the larger extent of melting-related parameter sensitivity (Fig. B.17) compared to q_v as well as the large extent of evaporation-related sensitivity compared to lh. The spatial extent and altitude of melting-related sensitivities suggests that it is particularly relevant in regions where strong vertical winds move warm air up and merge with frozen hydrometeors. Similar to lh, the area of influence for the fall-velocity related parameter is larger than the analysis for q_v. This is broadly consistent with the role of the different processes for lc, lh, and q_v.

6. Impact of WCB ascent timescale

Aside from air temperature, which constrains the possible (meta-)stable states of water in an air parcel, vertical velocity is known to be of fundamental importance for the subset of active cloud microphysical

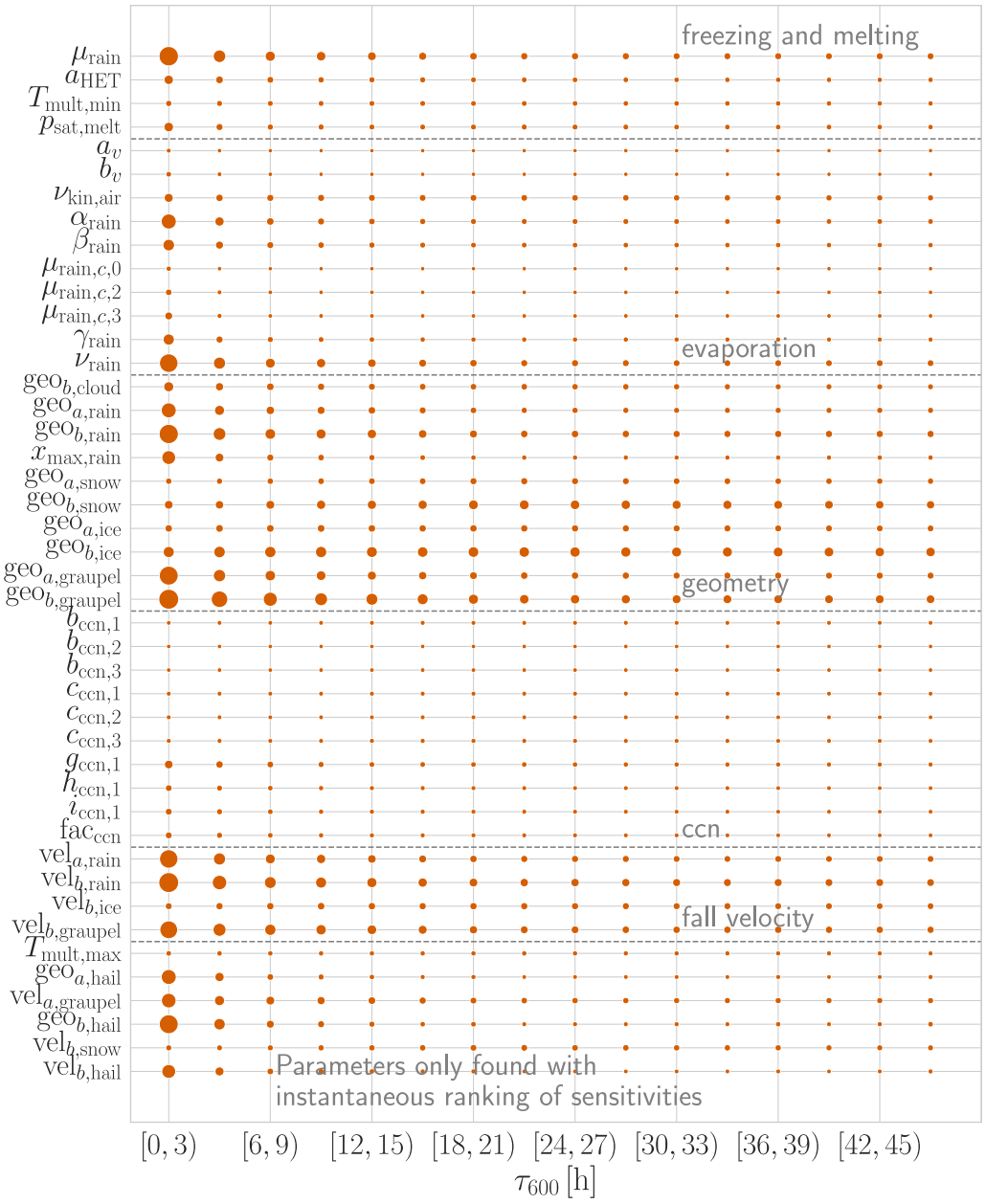

Fig. 13. Mean gradients $\overline{|\xi^p_{t^*,j,lh}|}$ for latent heating with different ascent timescales (τ_{600}) of the trajectories. The size of the markers is proportional to the mean of each gradient.

processes and the hydrometeors carried by an air parcel. Recent studies have highlighted the large spread of vertical velocities in WCB ascent ranging from convective type ascent (vertical velocity ∼1 to $10\,\text{m}\,\text{s}^{-1}$) to slantwise ascent (vertical velocity ∼$1\,\text{cm}\,\text{s}^{-1}$) [e.g. 33,52]. It has been further shown that the cloud microphysical evolution and precipitation-formation processes differ between quickly and slowly ascending air parcels [e.g. 52,57]. Therefore, we compare the leading-order parameter sensitivities for trajectories with different ascent timescales τ_{600} (defined in Section 2.1). The leading order processes for lh along with the mean sensitivity are shown in Fig. 13 for different ascent timescales (for q_v and ls see Figs. A.14 and A.15). The strongest sensitivities across all τ_{600} are found for parameters related to particle geometry and fall velocity followed by freezing/melting, evaporation, and CCN activation, i.e., consistent with results presented in the two previous sections.

The number of leading order parameters with large mean sensitivity is largest for trajectories with short τ_{600} ($\lesssim 9\,h$) and decreases for more slantwise ascending parcels. The mean sensitivity decreases for most parameters with increasing τ_{600}. This is most pronounced for parameters related to graupel and hail mass-diameter relation and fallspeed. In addition, this also holds for parameters related to rain freezing and rain evaporation. Graupel and hail are typically only found in regions of embedded convection, where vertical velocities are large enough to sustain supercooled liquid to cold temperatures and keep larger hydrometeors airborne [57]. This also explains the stronger sensitivities to parameters related to rain-freezing in fast ascending trajectories. Interestingly, parameters relating to the geometry of snow display larger mean sensitivity for mid-range τ_{600} (18–36 h). For the slantwise ascending trajectories, depositional growth of ice and snow has been suggested to be more important [57]. Parameters in the snow mass-diameter relation appear in the depositional growth description, contributing additional latent heating in the mixed-phase cloud regime. The larger parameter sensitivity is therefore consistent

with the physical understanding of the tau_{600} dependence of cloud processes.

Mean parameter sensitivities for q_v are larger for parameters related to evaporation and smaller for graupel and hail, as well as freezing/melting related parameters again in-line with discussion in previous sections (Fig. A.14). In contrast to lh, mean sensitivities are not showing a strong decrease with τ_{600}, while a small local maximum at mid-range τ_{600} remains for parameters related to rain and snow geometry. This likely is down to q_v being strongly controlled by the saturation adjustment assumption during the majority of the ascent independent of τ_{600} (up until full glaciation). At the same time, lh is modulated by additional heat release from freezing. Full glaciation in slantwise ascending trajectories is typically reached at warmer temperatures than in fast ascending trajectories [57]. Amongst others, the glaciation temperature is influenced by the efficiency of vapor deposition and removal of liquid by rain formation and riming. Again, the physical insight into controlling processes is consistent with the τ_{600} dependence of parameter sensitivity found in our analysis. In summary, substantial differences in parameter sensitivity are found between different WCB ascent regimes, which introduce variability in the spatio-temporal patterns of parameter sensitivity on top of the thermodynamically controlled variability.

Finally, mean parameter sensitivities for lc are again more similar to the results for lh, but with a stronger emphasis on parameters related to melting, rain mass-diameter relation and fallspeed (connected to evaporation), and graupel geometry.

7. Concluding discussion

We performed a systematic sensitivity analysis of 169 microphysical parameters in the two-moment microphysics scheme of the ICON model, which is computationally feasible through AD. AD efficiently and simultaneously estimates the sensitivities of the model state to several pre-defined uncertain parameters. The sensitivity analysis was applied to q_v, lh, and lc along more than 16,000 trajectories within the strongly ascending WCB airstream. These target variables have been chosen for their link to thermal stratification and parcel temperature, which impacts local vertical velocity as well as via its impact on potential vorticity distribution on the cyclone evolution itself.

We use the leading order of magnitude for each trajectory, different cloud phases, and a threshold based on the fraction of data points, yielding 38 relevant uncertain parameters. The 38 parameters are associated with only a few microphysical processes, primarily rain evaporation, diameter-mass and fall velocity relations for hydrometeors, CCN activation, frozen hydrometeor melting, and rain freezing.

The sensitivities systematically differ depending on the target variables (q_v, lh, and lc). For any given target, the leading order parameters vary systematically with cloud phase, WCB ascent stage (inflow, strong ascent, outflow), and ascent timescale τ_{600}. These dependencies are largely consistent with a general understanding of dominant cloud microphysical processes in the different regimes. In summary:

- q_v is mainly sensitive to parameters used for rain evaporation and CCN activation, followed by those used in diameter-mass relations of frozen hydrometers. The former dominates in warm-phase cloud segments and WCB inflow. At the same time, parameters related to the geometry of frozen hydrometeors are important in mixed-phase cloud segments and the strong ascent region. Parameter sensitivity in the ice-phase segments and the outflow are dominated by those related to ice geometry and fallspeed. q_v sensitivity does not vary much with τ_{600} likely due to the strong assumption of saturation adjustment.
- The largest parameter sensitivities for lh are found in mixed-phase cloud segments and strong ascent regions. They relate to frozen hydrometeor geometry, fall velocity, and rain freezing. These parameters impact the representation of depositional growth and riming, i.e., processes controlling liquid/ice partitioning and, thereby, additional latent heat release from freezing. Additionally, weaker sensitivity to CCN activation related parameters is found in the warm-phase/inflow region and to ice geometry-related parameters in the ice-phase/outflow region. For most leading order parameters, sensitivities are largest in fast-rising air parcels ($\tau_{600} \leq 9\,h$).
- The largest parameter sensitivities for lc are related to parameters used to describe melting, rain evaporation, and the diameter-mass relation of rain, graupel, and ice. Sensitivity to rain evaporation occurs predominantly in the warm-phase/inflow region, while melting-related sensitivity is largest in mixed-phase/strong ascent regions. In the ice-phase/outflow region, there is some (small) sensitivity to parameters used to describe ice geometry. Similar to lh, parameter sensitivities are largest for fast-rising parcels.

The parameter sensitivities identified by AD are local gradients in the model state. As the highly non-linear processes governing cloud evolution can potentially amplify and buffer local deviations in the microphysical state, parameter sensitivities may only be important if they occur consistently over a "long" time span or a "larger" geographic region. Very short-lived or local parameter sensitivities are hypothesized not to impact cloud evolution over a longer time period. To elucidate the spatio-temporal structure of AD-derived gradients, we have first investigated the temporal persistence of individual parameters being in leading order for individual trajectories. Indeed, we found a large persistence of these dominating parameter sensitivities for many, but not all, parameters with large local gradients. The Lagrangian information about parameters dominating parameter sensitivity has then been mapped to the Eulerian domain to retrieve the spatial extent and lifetime of patches, over which a specific parameter coherently dominates sensitivity, i.e., is leading order. For most key parameters, several patches extending over a large fraction of the horizontal extent of the WCB object and more than 10 h have been identified over the WCB lifecycle. However, the analysis of the Eulerian projection also confirmed spatial (and, to a lesser degree, temporal) variability in the parameters dominating the sensitivity of the model state. The most prominent variations occur with altitude, where at the lowest altitudes, parameters related to rain evaporation and rain size distribution dominate, followed by those related to CCN activation and melting. In the mid-troposphere, parameters related to the geometry of frozen hydrometeors and freezing dominate, and those related to ice geometry and fall velocity dominate in the upper troposphere. This broadly reflects the variability of leading order parameters with the cloud phase. In addition, horizontal variability in leading order parameters is found at any given altitude level, which is most pronounced in the lower troposphere. For example, horizontal bands of high sensitivity to rain evaporation occur below 800 hPa. We hypothesize that this horizontal variability may be related to the distribution of τ_{600} trajectories and embedded convection.

The spatio-temporal consistency of leading order parameter sensitivities, as identified by AD, suggests that the identified parameters are indeed very relevant for the future cloud microphysical evolution. This is further supported by the similarity in the ranking of parameter impact from AD-derived sensitivity and Monte-Carlo type ensembles of Lagrangian cloud evolution reported by Hieronymus et al. [13]. To what extent this holds for interactive simulations of the cloud microphysical evolution, where cloud microphysical processes and dynamics are fully coupled, bears further investigation. For example, it remains open to whether and how the parameter uncertainty related to rain evaporation in the lower troposphere influences subsequent WCB ascent. WCB trajectories starting in a region with enhanced rain evaporation may ascent earlier and/or faster, triggered by earlier

condensational heating as saturated conditions in cooler and moister conditions are reached earlier.

Furthermore, future studies with fully interactive NWP models need to corroborate further the extent to which all relevant parameters are identified and if the parameter selection approach here suffices. For example, CCN activation mainly occurs only over a very shallow region at the cloud base but influences the cloud evolution over a large time span. This will require a very careful design of the target variables for which gradients are derived and the criteria used for parameter ranking and selection. This must include interdependencies between parameter values that are not reflected in the model formulation but are inherent in the underlying physics and equations. For example, the various parameters in the CCN activation are not independent, similar to those used in the mass-diameter and diameter-fallspeed relations. Although AD cannot directly provide answers to such questions, the present analysis suggests it is a useful and promising tool for efficiently, simultaneously, and systematically identifying the most relevant parameters from a very large parameter space, efficiently narrowing down the remaining relevant parameter space for subsequent analyses.

The methods and results presented here can contribute to further model improvement and ensemble simulation enhancement:

- **Model improvement**
  - Combine parameter uncertainty with AD-estimated sensitivities to identify processes with the highest potential for increased accuracy, i.e., by improving their representation using more accurate empirical relationships.
  - Simplify less influential parameterizations to optimize model complexity and reduce computational cost.
  - Analyze different schemes and case studies to guide refinements in a generalizable way.
- **Ensemble simulation enhancement**
  - Use AD-estimated sensitivities to get an objective parameter selection for fully perturbed ensemble simulations.
  - Dynamically apply adaptive perturbation based on AD-estimated sensitivities throughout the simulation.

AD can guide model refinements in a generalizable manner if common parameters or processes emerge as influential across different cases. AD remains valuable in guiding improvements when analyzing multiple models or schemes if common physical processes emerge as dominant. However, whether results are transferable between different schemes remains an open question for future research. While model refinements aim to increase the accuracy of weather forecasts, enhancing ensemble simulations addresses their underdispersiveness. An overconfident prediction may miss extreme weather events or the severity of high-impact events that are expected to increase in frequency and intensity due to climate change. Hieronymus et al. [13] demonstrated that parameters with the highest sensitivities correlate with ensemble spread. Accordingly, our tool provides a means to estimate the uncertainty of forecasts more accurately.

In summary, AD is a powerful and systematic approach for identifying key sensitivities in cloud microphysics. As NWP models move toward increasingly higher resolutions with the increase in computational power, the impact of cloud microphysics schemes becomes more critical. We propose integrating AD-based insights into future research to enhance the accuracy of cloud parameterizations while addressing challenges like underdispersiveness in ensemble simulations, ultimately contributing to more reliable weather predictions.

CRediT authorship contribution statement

Maicon Hieronymus: Writing – original draft, Visualization, Validation, Software, Methodology, Investigation, Formal analysis, Data curation, Conceptualization. **Annika Oertel:** Writing – original draft, Visualization, Resources, Conceptualization. **Annette K. Miltenberger:** Writing – review & editing, Writing – original draft, Supervision, Conceptualization. **André Brinkmann:** Writing – review & editing, Supervision, Project administration, Funding acquisition.

Declaration of competing interest

The authors declare the following financial interests/personal relationships which may be considered as potential competing interests: Maicon Hieronymus reports financial support, administrative support, equipment, drugs, or supplies, and travel were provided by Deutsche Forschungsgemeinschaft (DFG) within the Transregional Collaborative Research Centre TRR165 Waves to Weather. Annika Oertel reports administrative support was provided by Italia - Deutschland science-4-services network in weather and climate (IDEA-S4S; INVACODA, 4823IDEAP6). This Italian-German research network of universities, research institutes and Deutscher Wetterdienst is funded by the BMDV (Federal Ministry of Digital and Transport). Work was also performed on the HoreKa supercomputer funded by the Ministry of Science, Research and the Arts Baden- Württemberg and by the Federal Ministry of Education and Research by Annika Oertel. The other authors declare that they have no known competing financial interests or personal relationships that could have appeared to influence the work reported in this paper.

Acknowledgment

Parts of this research were conducted using the supercomputer Mogon II and auxiliary services offered by Johannes Gutenberg University Mainz (hpc.uni-mainz.de), which is a member of the AHRP and the Gauss Alliance e.V. The authors kindly acknowledge support by the state of Baden-Württemberg through bwHPC. The PPE simulations were carried out on the supercomputer HoreKa at Karlsruhe Institute of Technology, Karlsruhe, which is funded by the Ministry of Science, Research and the Arts Baden-Württemberg, Germany, and the German Federal Ministry of Education and Research. The research leading to these results has been done within the subprojects Z2 and B8 of the Transregional Collaborative Research Center SFB/TRR 165 “Waves to Weather” (www.wavestoweather.de) funded by the German Research Foundation (DFG). Annika Oertel is supported by the Italia–Deutschland science-4-services network in weather and climate (IDEA-S4S; INVACODA, grant no. 4823IDEAP6). This Italian–German research network of universities, research institutes, and the Deutscher Wetterdienst is funded by the BMDV (Federal Ministry of Transport and Digital Infrastructure). This open-access publication was funded by Johannes Gutenberg University Mainz.

Appendix A. Mean gradients with different timescales

See Figs. A.14 and A.15.

Appendix B. Frequency distribution of sensitive coherent regions

See Figs. B.16 and B.17.

Appendix C. Parameter details

See Tables C.3–C.9.

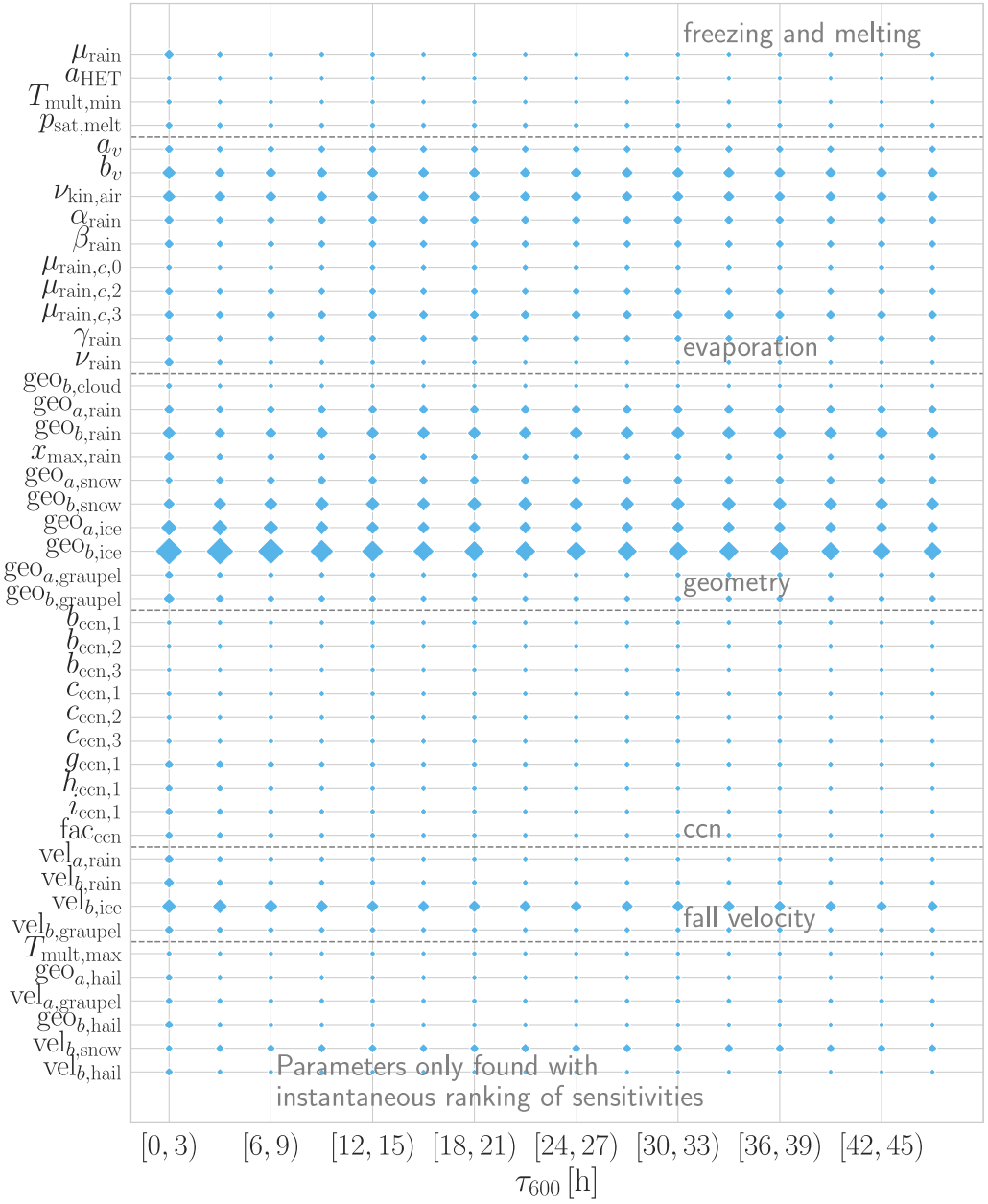

Fig. A.14. Mean gradients $\overline{|\zeta^p_{i^*,i,q_v}|}$ for specific humidity with different ascent timescales (τ_{600}) of the trajectories. The size of the markers is proportional to the mean of each gradient.

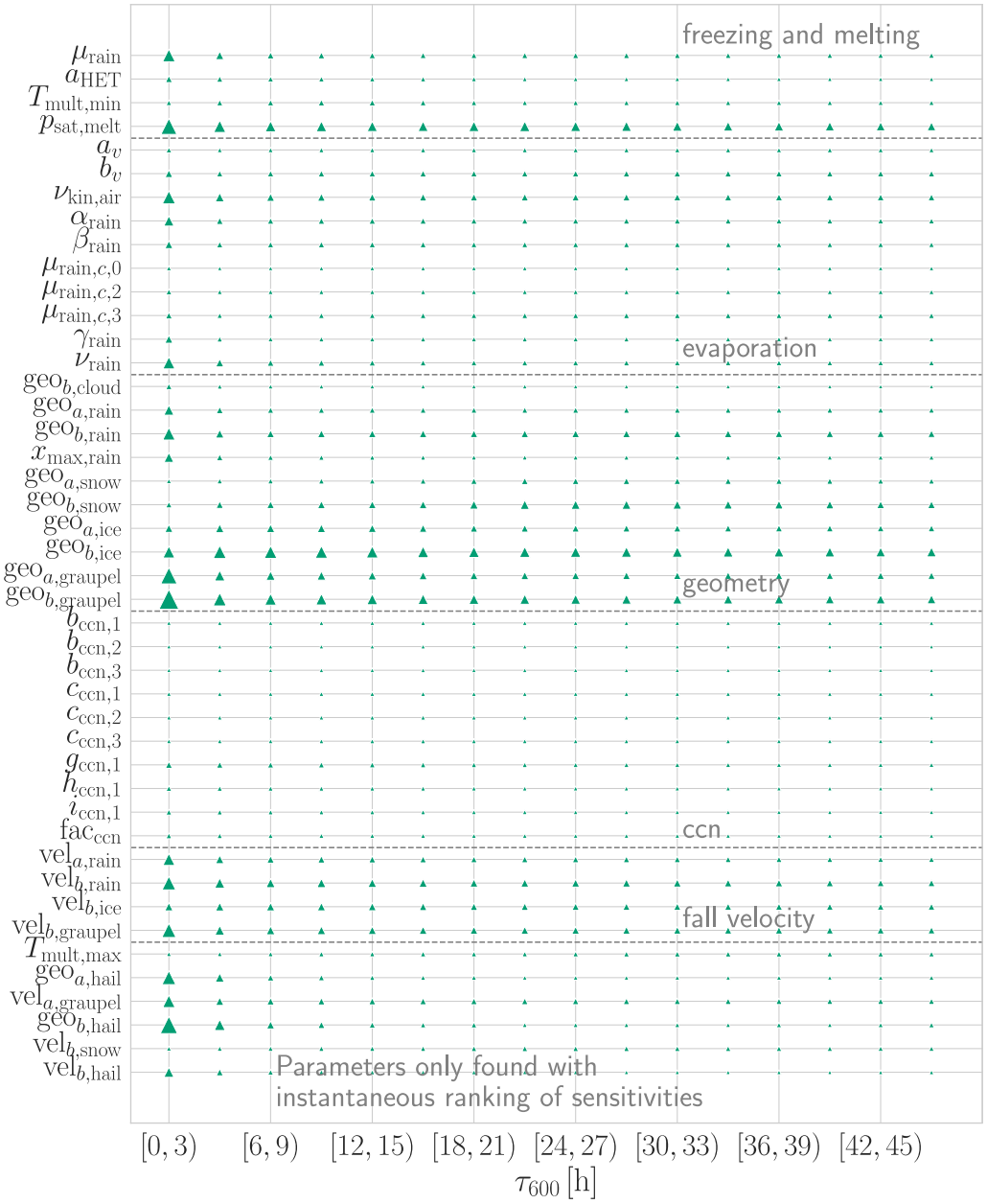

Fig. A.15. As Fig. A.14 but for latent cooling.

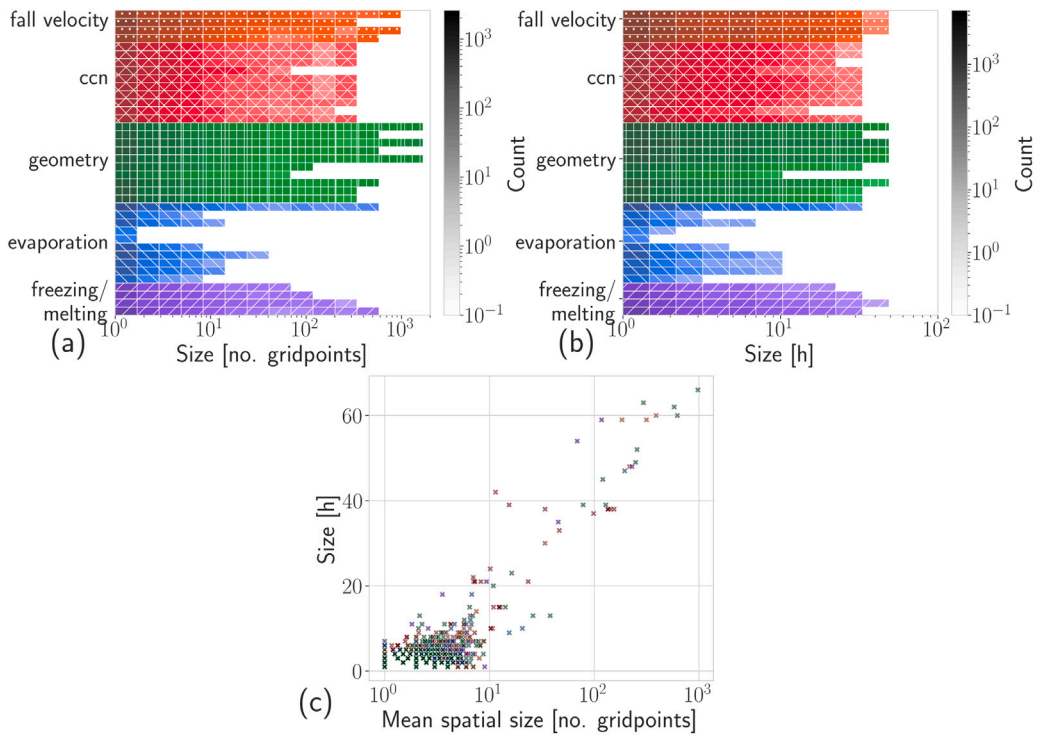

Fig. B.16. Frequency distribution of spatio-temporal dimension of coherent regions with non-zero sensitivity for *lh*: **(a)** spatial extend in the number of gridpoints (regridded data), **(b)** temporal extend in hours, **(c)** correlation of object spatial and temporal extend.

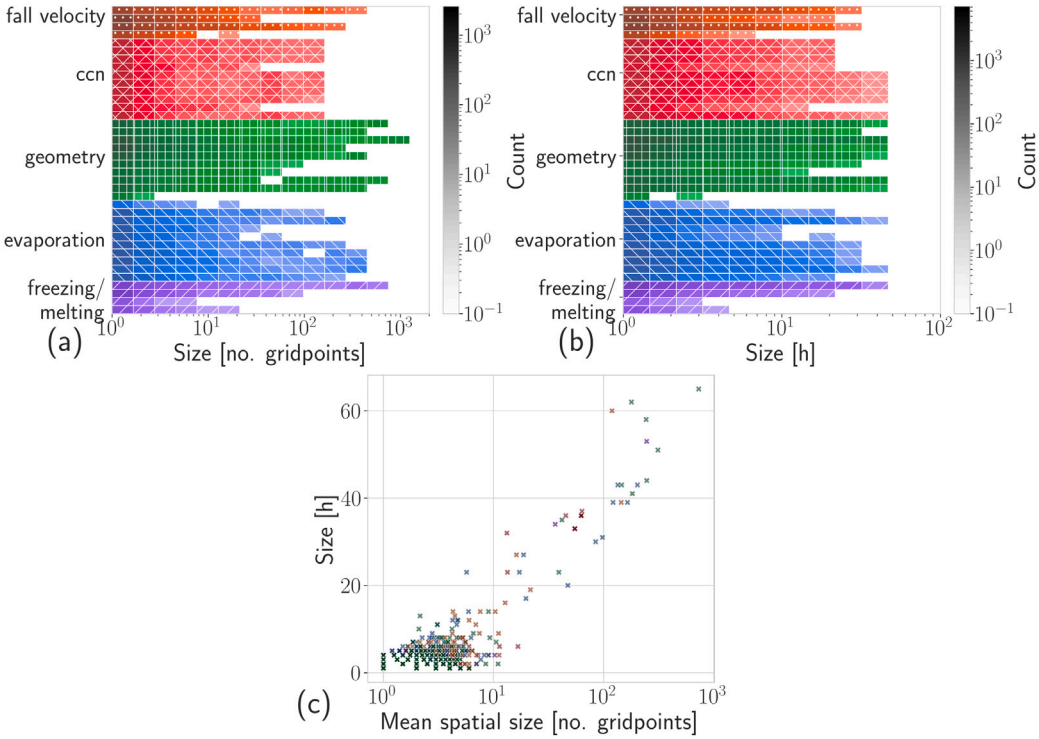

Fig. B.17. Frequency distribution of spatio-temporal dimension of coherent regions with non-zero sensitivity for *lc*: **(a)** spatial extend in the number of gridpoints (regridded data), **(b)** temporal extend in hours, **(c)** correlation of object spatial and temporal extend.

Table C.3
The parameters identified as important with the approach by [13], modified by stratifying for cloud phases and our approach. Bold parameters are important for water vapor.

Top Parameters [13]	Top Parameters Hieronymus et al. [13] with cloud phases	Top Parameters Our method
fall velocity	*fall velocity*	*fall velocity*
$\mathrm{vel}_{a,\mathrm{rain}}$, $\mathrm{vel}_{b,\mathrm{rain}}$, $\mathrm{vel}_{b,\mathrm{ice}}$	$\mathrm{vel}_{a,\mathrm{rain}}$, $\mathrm{vel}_{b,\mathrm{rain}}$, $\mathrm{vel}_{b,\mathrm{ice}}$	$\mathrm{vel}_{a,\mathrm{rain}}$, $\mathrm{vel}_{b,\mathrm{rain}}$, $\mathbf{vel_b, ice}$
$\mathrm{vel}_{b,\mathrm{graupel}}$	$\mathrm{vel}_{b,\mathrm{graupel}}$	$\mathrm{vel}_{b,\mathrm{graupel}}$
ccn	*ccn*	*ccn*
	$b_{\mathrm{ccn},1}$, $b_{\mathrm{ccn},2}$, $b_{\mathrm{ccn},3}$, $c_{\mathrm{ccn},1}$	$\mathbf{b_{ccn},1}$, $\mathbf{b_{ccn},2}$, $\mathbf{b_{ccn},3}$, $\mathbf{c_{ccn},1}$
	$c_{\mathrm{ccn},2}$, $c_{\mathrm{ccn},3}$, $g_{\mathrm{ccn},1}$, $h_{\mathrm{ccn},1}$	$\mathbf{c_{ccn},2}$, $\mathbf{c_{ccn},3}$, $\mathbf{g_{ccn},1}$, $\mathbf{h_{ccn},1}$
	$i_{\mathrm{ccn},1}$, $\mathrm{fac}_{\mathrm{ccn}}$	$\mathbf{i_{ccn},1}$, $\mathbf{fac_{ccn}}$
geometry	*geometry*	*geometry*
$\mathbf{geo_{b,rain}}$	$\mathbf{geo_{a,rain}}$, $\mathbf{geo_{b,rain}}$	$\mathrm{geo}_{b,\mathrm{cloud}}$, $\mathbf{geo_{a,rain}}$, $\mathbf{geo_{b,rain}}$
$\mathbf{geo_{b,snow}}$	$\mathbf{geo_{b,snow}}$	$\mathbf{x_{a,rain}}$, $\mathbf{geo_{a,snow}}$, $\mathbf{geo_{b,snow}}$
$\mathbf{geo_{a,ice}}$, $\mathbf{geo_{b,ice}}$	$\mathbf{geo_{a,ice}}$, $\mathbf{geo_{b,ice}}$	$\mathbf{geo_{a,ice}}$, $\mathbf{geo_{b,ice}}$
$\mathrm{geo}_{a,\mathrm{graupel}}$, $\mathrm{geo}_{b,\mathrm{graupel}}$	$\mathrm{geo}_{a,\mathrm{graupel}}$, $\mathrm{geo}_{b,\mathrm{graupel}}$	$\mathrm{geo}_{a,\mathrm{graupel}}$, $\mathrm{geo}_{b,\mathrm{graupel}}$
evaporation	*evaporation*	*evaporation*
$\mathbf{b_v}$, $\mathbf{\nu_{kin,air}}$	$\mathbf{b_a}$, $\mathbf{\nu_{kin,air}}$, $\mathbf{\alpha_{rain}}$	$\boldsymbol{a_v}$, $\mathbf{b_v}$, $\mathbf{\nu_{kin,air}}$, $\mathbf{\alpha_{rain}}$
	$\mathbf{\beta_{rain}}$	$\mathbf{\beta_{rain}}$, $\mathbf{\mu_{rain},c,0}$
	$\mathbf{\mu_{rain},c,3}$	$\mathbf{\mu_{rain},c,2}$, $\mathbf{\mu_{rain},c,3}$
ν_{rain}	ν_{rain}	$\mathbf{\gamma_{rain}}$, ν_{rain}
freezing and melting	*freezing and melting*	*freezing and melting*
μ_{rain}, $p_{\mathrm{sat,melt}}$	μ_{rain}, $p_{\mathrm{sat,melt}}$	μ_{rain}, a_{HET}, $T_{\mathrm{mult,min}}$, $p_{\mathrm{sat,melt}}$

Table C.4
The set of top model parameters grouped in 'freezing and melting'.

Model parameter	Description
μ_{rain}	Defines the shape of the generalized Γ-distribution, applied to model the freezing behavior of rain.
a_{HET}	Exponent for heterogeneous rain freezing with data of Barklie and Gokhale used in freezing of rain.
$T_{\mathrm{mult,min}}$	Coefficient used in Hallet–Mossop ice multiplication.
$p_{\mathrm{sat,melt}}$	Saturation pressure at $\mathrm{T} = \mathrm{T}_{\mathrm{freeze}}$ used to model the melting of snow, graupel, and hail.

Table C.5
The set of top model parameters grouped in 'evaporation'.

Model Parameter	Description
a_v	Constant used in calculating the ventilation factor during rain evaporation.
b_v	Coefficient used in calculating the ventilation factor during rain evaporation.
$\nu_{\mathrm{kin,air}}$	Kinematic viscosity of dry air used to calculate the terminal fall velocity of rain during rain evaporation.
α_{rain}	Constant in rain sedimentation.
β_{rain}	Coefficient for rain sedimentation.
$\mu_{\mathrm{rain},c,0}$	Coefficient for calculating the shape parameter μ during rain evaporation and sedimentation.
$\mu_{\mathrm{rain},c,2}$	Coefficient for calculating the shape parameter μ during rain evaporation and sedimentation.
$\mu_{\mathrm{rain},c,3}$	Constant for calculating the shape parameter μ during rain evaporation and sedimentation.
γ_{rain}	Exponent applied in rain sedimentation.
ν_{rain}	Parameter defining the shape of the generalized Γ-distribution for rain sedimentation.

Table C.6
The set of top model parameters grouped in 'geometry'.

Model Parameter	Description
$\text{geo}_{b,\text{cloud}}$	Exponent for diameter size calculation of cloud droplets applied in riming processes.
$\text{geo}_{a,\text{rain}}$	Coefficient for diameter size calculation of raindrops applied in rain collision, evaporation, sedimentation, riming, and rain freezing.
$\text{geo}_{b,\text{rain}}$	Exponent for diameter size calculation of raindrops applied in rain collision, evaporation, sedimentation, riming, and rain freezing.
$x_{\text{max,rain}}$	Maximum (mean) size of raindrop used during rain collision, evaporation, sedimentation, riming, and freezing.
$\text{geo}_{a,\text{snow}}$	Coefficient used to calculate the diameter of snow particles.
$\text{geo}_{b,\text{snow}}$	Exponent used to calculate the diameter of snow particles.
$\text{geo}_{a,\text{ice}}$	Coefficient used to determine the diameter of ice particles.
$\text{geo}_{b,\text{ice}}$	Exponent used to determine the diameter of ice particles.
$\text{geo}_{a,\text{graupel}}$	Coefficient for diameter size calculation of graupel.
$\text{geo}_{b,\text{graupel}}$	Exponent for diameter size calculation of graupel.

Table C.7
The set of top model parameters grouped in 'ccn'. CCN activation is used as in Oertel et al. [33], which is based on Hande et al. [61].

Model Parameter	Description
$b_{\text{ccn},1}$	Parameter for calculating CCN concentration during CCN activation.
$b_{\text{ccn},2}$	Parameter for calculating CCN concentration during CCN activation.
$b_{\text{ccn},3}$	Parameter for calculating CCN concentration during CCN activation.
$c_{\text{ccn},1}$	Parameter for calculating CCN concentration during CCN activation.
$c_{\text{ccn},2}$	Parameter for calculating CCN concentration during CCN activation.
$c_{\text{ccn},3}$	Parameter for calculating CCN concentration during CCN activation.
$g_{\text{ccn},1}$	Baseline pressure reference for determining CCN concentration.
$h_{\text{ccn},1}$	Multiplicative factor contributing to calculate the CCN concentration.
$i_{\text{ccn},1}$	Scaling factor for the overall impact of CCN activation.
fac_{ccn}	Scaling factor for the overall impact of CCN activation.

Table C.8
The set of top model parameters grouped in 'fall velocity'.

Model parameter	Description
$\text{vel}_{a,\text{rain}}$	Coefficient for determining the fall velocity of rain during riming.
$\text{vel}_{b,\text{rain}}$	Exponent for the fall velocity of rain, used in riming.
$\text{vel}_{b,\text{ice}}$	Exponent for calculating the fall velocity of ice particles, applied in collision, sedimentation, evaporation, and riming processes.
$\text{vel}_{b,\text{graupel}}$	Exponent for the fall velocity of graupel, used in melting, sedimentation, evaporation, collision of hydrometeors, and riming.

Table C.9
The model parameters with sensitivity in the top magnitude for each model state variable and phase for at least 0.1% of all relevant time steps. The parameters are sorted by the number of times they are in the leading order of magnitude.

Model state variable	Phase	Top parameters
Water Vapor Mass Density	warm-phase	$\text{geo}_{b,\text{rain}}$, b_v, α_{rain}, $\nu_{\text{kin,air}}$ $\text{geo}_{a,\text{rain}}$, β_{rain}, $\mu_{\text{rain},c,3}$, a_v, $c_{\text{ccn},3}$, $c_{\text{ccn},1}$, $c_{\text{ccn},2}$, $b_{\text{ccn},1}$, fac_{ccn}, $i_{\text{ccn},1}$, γ_{rain}, $h_{\text{ccn},1}$, $b_{\text{ccn},3}$, $x_{\text{max,rain}}$, $g_{\text{ccn},1}$, $\mu_{\text{rain},c,0}$, $\mu_{\text{rain},c,2}$, $b_{\text{ccn},2}$
Latent Heating	warm-phase	$c_{\text{ccn},3}$, $c_{\text{ccn},1}$, $c_{\text{ccn},2}$, $b_{\text{ccn},1}$, fac_{ccn}, $i_{\text{ccn},1}$, $h_{\text{ccn},1}$, $b_{\text{ccn},3}$, $g_{\text{ccn},1}$, $b_{\text{ccn},2}$
Latent Cooling	warm-phase	$\text{geo}_{b,\text{rain}}$, b_v, α_{rain}, $\nu_{\text{kin,air}}$, $\text{geo}_{a,\text{rain}}$, β_{rain}, $\mu_{\text{rain},c,3}$, a_v, γ_{rain}, $c_{\text{ccn},3}$, $b_{\text{ccn},1}$, $c_{\text{ccn},1}$, $c_{\text{ccn},2}$, $x_{\text{max,rain}}$, fac_{ccn}, $i_{\text{ccn},1}$, $h_{\text{ccn},1}$, $b_{\text{ccn},3}$, $\mu_{\text{rain},c,0}$, $\mu_{\text{rain},c,2}$, $g_{\text{ccn},1}$
Water Vapor Mass Density	mixed-phase	$\text{geo}_{b,\text{ice}}$, $\text{geo}_{b,\text{rain}}$, $\text{geo}_{b,\text{snow}}$, b_v, $\mu_{\text{rain},c,3}$, $\text{geo}_{a,\text{rain}}$, $\nu_{\text{kin,air}}$, $\text{geo}_{a,\text{ice}}$
Latent Heating	mixed-phase	$\text{geo}_{b,\text{ice}}$, $\text{geo}_{b,\text{graupel}}$, $\text{geo}_{b,\text{snow}}$, $\text{vel}_{b,\text{rain}}$, $\text{vel}_{b,\text{graupel}}$, $\text{geo}_{b,\text{rain}}$, $\text{geo}_{a,\text{graupel}}$, μ_{rain}, $\text{vel}_{a,\text{rain}}$, $\text{geo}_{a,\text{ice}}$, ν_{rain}, $\text{vel}_{b,\text{ice}}$, $\text{geo}_{a,\text{rain}}$, a_{HET}, $\text{geo}_{a,\text{snow}}$, $\text{geo}_{b,\text{cloud}}$, $T_{\text{mult,min}}$, $p_{\text{sat,melt}}$
Latent Cooling	mixed-phase	$\text{geo}_{b,\text{ice}}$, $\text{geo}_{b,\text{graupel}}$, $p_{\text{sat,melt}}$, $\text{geo}_{b,\text{snow}}$, $\text{geo}_{b,\text{rain}}$, $\text{geo}_{a,\text{graupel}}$, b_v, $\text{vel}_{b,\text{graupel}}$, $\text{vel}_{b,\text{rain}}$, $\text{geo}_{a,\text{ice}}$, $\text{geo}_{a,\text{rain}}$, $\mu_{\text{rain},c,3}$, $\text{geo}_{a,\text{snow}}$, $\nu_{\text{kin,air}}$, $\text{vel}_{b,\text{ice}}$
Water Vapor Mass Density	ice-phase	$\text{geo}_{b,\text{ice}}$, $\text{geo}_{a,\text{ice}}$, $\text{geo}_{b,\text{snow}}$, $\text{vel}_{b,\text{ice}}$, $\text{geo}_{a,\text{snow}}$
Latent Heating	ice-phase	$\text{geo}_{b,\text{ice}}$, $\text{geo}_{a,\text{ice}}$, $\text{geo}_{b,\text{snow}}$, $\text{vel}_{b,\text{ice}}$, $\text{geo}_{a,\text{snow}}$
Latent Cooling	ice-phase	$\text{geo}_{b,\text{ice}}$, $\text{geo}_{a,\text{ice}}$, $\text{geo}_{b,\text{snow}}$, $\text{vel}_{b,\text{ice}}$, $\text{geo}_{a,\text{snow}}$

Data availability

The ICON source code is distributed under the BSD-3-C license license issued by the German Weather Service (DWD). For more information, see https://code.mpimet.mpg.de/projects/iconpublic (DWD and MPI, 2015). The WCB online trajectories and sensitivities are available from [60]. The code to compute the microphysical sensitivities and to select the most important parameters is available from [62].

We provide three videos to show the evolution of the area of parameters, which are most often leading order of magnitude for different heights [60]. Gray areas are bins without any parameters in leading order, and those indicate the area covered by our simulation.

References

[1] R. Buizza, M. Milleer, T.N. Palmer, Stochastic representation of model uncertainties in the ECMWF ensemble prediction system, Q. J. R. Meteorol. Soc. 125 (560) (1999) 2887–2908, http://dx.doi.org/10.1002/qj.49712556006.

[2] P. Ollinaho, S.-J. Lock, M. Leutbecher, P. Bechtold, A. Beljaars, A. Bozzo, R.M. Forbes, T. Haiden, R.J. Hogan, I. Sandu, Towards process-level representation of model uncertainties: stochastically perturbed parametrizations in the ECMWF ensemble, Q. J. R. Meteorol. Soc. 143 (702) (2017) 408–422, http://dx.doi.org/10.1002/qj.2931.

[3] S.T.K. Lang, S.-J. Lock, M. Leutbecher, P. Bechtold, R.M. Forbes, Revision of the Stochastically Perturbed Parametrisations model uncertainty scheme in the Integrated Forecasting System, Q. J. R. Meteorol. Soc. 147 (735) (2021) 1364–1381, http://dx.doi.org/10.1002/qj.3978.

[4] M. Leutbecher, S.-J. Lock, P. Ollinaho, S.T.K. Lang, G. Balsamo, P. Bechtold, M. Bonavita, H.M. Christensen, M. Diamantakis, E. Dutra, S. English, M. Fisher, R.M. Forbes, J. Goddard, T. Haiden, R.J. Hogan, S. Juricke, H. Lawrence, D. MacLeod, L. Magnusson, S. Malardel, S. Massart, I. Sandu, P.K. Smolarkiewicz, A. Subramanian, F. Vitart, N. Wedi, A. Weisheimer, Stochastic representations of model uncertainties at ECMWF: state of the art and future vision, Q. J. R. Meteorol. Soc. 143 (707) (2017) 2315—2339, http://dx.doi.org/10.1002/qj.3094.

[5] T. Matsunobu, M. Puh, C. Keil, Flow- and scale-dependent spatial predictability of convective precipitation combining different model uncertainty representations, Q. J. R. Meteorol. Soc. 150 (761) (2024) 2364–2381, http://dx.doi.org/10.1002/qj.4713.

[6] K.A. Peterson, G.C. Smith, J.-F. Lemieux, F. Roy, M. Buehner, A. Caya, P.L. Houtekamer, H. Lin, R. Muncaster, X. Deng, F. Dupont, N. Gagnon, Y. Hata, Y. Martinez, J.S. Fontecilla, D. Surcel-Colan, Understanding sources of Northern Hemisphere uncertainty and forecast error in a medium-range coupled ensemble sea-ice prediction system, Q. J. R. Meteorol. Soc. 148 (747) (2022) 2877–2902, http://dx.doi.org/10.1002/qj.4340.

[7] F. Jansson, M. Janssens, J.H. Grönqvist, A.P. Siebesma, F. Glassmeier, J. Attema, V. Azizi, M. Satoh, Y. Sato, H. Schulz, T. Kölling, Cloud Botany: Shallow Cumulus Clouds in an Ensemble of Idealized Large-Domain Large-Eddy Simulations of the Trades, J. Adv. Model. Earth Syst. 15 (11) (2023) http://dx.doi.org/10.1029/2023MS003796, e2023MS003796.

[8] R.E. Hawker, A.K. Miltenberger, J.S. Johnson, J.M. Wilkinson, A.A. Hill, B.J. Shipway, P.R. Field, B.J. Murray, K.S. Carslaw, Model emulation to understand the joint effects of ice-nucleating particles and secondary ice production on deep convective anvil cirrus, Atmos. Chem. Phys. 21 (23) (2021) 17315–17343, http://dx.doi.org/10.5194/acp-21-17315-2021.

[9] C. Wellmann, A.I. Barrett, J.S. Johnson, M. Kunz, B. Vogel, K.S. Carslaw, C. Hoose, Comparing the impact of environmental conditions and microphysics on the forecast uncertainty of deep convective clouds and hail, Atmos. Chem. Phys. 20 (4) (2020) 2201–2219, http://dx.doi.org/10.5194/acp-20-2201-2020, URL https://acp.copernicus.org/articles/20/2201/2020/.

[10] F. Glassmeier, F. Hoffmann, J.S. Johnson, T. Yamaguchi, K.S. Carslaw, G. Feingold, An emulator approach to stratocumulus susceptibility, Atmos. Chem. Phys. 19 (15) (2019) 10191–10203, http://dx.doi.org/10.5194/acp-19-10191-2019.

[11] L. Frey, C. Hoose, M. Kunz, A. Miltenberger, P. Kuntze, Using statistical emulation to quantify microphysical uncertainties for the Andreas hailstorm in 2013, in: EGU General Assembly Conference Abstracts, 2023, pp. EGU–14317, http://dx.doi.org/10.5194/egusphere-egu23-14317.

[12] J.S. Johnson, Z. Cui, L.A. Lee, J.P. Gosling, A.M. Blyth, K.S. Carslaw, Evaluating uncertainty in convective cloud microphysics using statistical emulation, J. Adv. Model. Earth Syst. 7 (1) (2015) 162–187, http://dx.doi.org/10.1002/2014MS000383.

[13] M. Hieronymus, M. Baumgartner, A. Miltenberger, A. Brinkmann, Algorithmic Differentiation for Sensitivity Analysis in Cloud Microphysics, J. Adv. Model. Earth Syst. 14 (7) (2022) http://dx.doi.org/10.1029/2021MS002849.

[14] M. Sagebaum, T. Albring, N.R. Gauger, High-performance derivative computations using CoDiPack, ACM Trans. Math. Software 45 (4) (2019) http://dx.doi.org/10.1145/3356900, URL https://doi.org/10.1145/3356900.

[15] A. Griewank, A. Walther, Evaluating Derivatives: Principles and Techniques of Algorithmic Differentiation, second ed., SIAM, 2008.

[16] C.H. Bischof, G.D. Pusch, R. Knoesel, Sensitivity analysis of the MM5 weather model using automatic differentiation, Comput. Phys. 10 (6) (1996) 605–612, http://dx.doi.org/10.1063/1.168585.

[17] C.H. Bischof, H.M. Bücker, A. Rasch, Sensitivity Analysis of Turbulence Models Using Automatic Differentiation, SIAM J. Sci. Comput. 26 (2) (2004) 510–522, http://dx.doi.org/10.1137/S1064827503426723.

[18] J.G. Kim, E.C. Hunke, W.H. Lipscomb, A Sensitivity-Enhanced Simulation Approach for Community Climate System Model, in: D. Hutchison, T. Kanade, J. Kittler, J.M. Kleinberg, F. Mattern, J.C. Mitchell, M. Naor, O. Nierstrasz, C. Pandu Rangan, B. Steffen, M. Sudan, D. Terzopoulos, D. Tygar, M.Y. Vardi, G. Weikum, V.N. Alexandrov, G.D. Van Albada, P.M.A. Sloot, J. Dongarra (Eds.), in: Computational Science – ICCS 2006, vol. 3994, Springer Berlin Heidelberg, Berlin, Heidelberg, 2006, pp. 533–540, http://dx.doi.org/10.1007/11758549_74.

[19] M. Gelbrecht, A. White, S. Bathiany, N. Boers, Differentiable programming for Earth system modeling, Geosci. Model. Dev. 16 (11) (2023) 3123–3135, http://dx.doi.org/10.5194/gmd-16-3123-2023.

[20] K. Um, R. Brand, Y.R. Fei, P. Holl, N. Thuerey, Solver-in-the-loop: Learning from differentiable physics to interact with iterative PDE-solvers, in: H. Larochelle, M. Ranzato, R. Hadsell, M. Balcan, H. Lin (Eds.), in: Adv. Neural Inf. Process. Syst., vol. 33, Curran Associates, Inc., 2020, pp. 6111–6122.

[21] D. Kochkov, J.A. Smith, A. Alieva, Q. Wang, M.P. Brenner, S. Hoyer, Machine learning –accelerated computational fluid dynamics, Proc. Natl. Acad. Sci. USA 118 (21) (2021) e2101784118, http://dx.doi.org/10.1073/pnas.2101784118.

[22] H. Frezat, J. Le Sommer, R. Fablet, G. Balarac, R. Lguensat, A Posteriori Learning for Quasi-Geostrophic Turbulence Parametrization, J. Adv. Model. Earth Syst. 14 (11) (2022) http://dx.doi.org/10.1029/2022MS003124, e2022MS003124.

[23] O. Martínez-Alvarado, E. Madonna, S.L. Gray, H. Joos, A route to systematic error in forecasts of Rossby waves, Q. J. R. Meteorol. Soc. 142 (694) (2016) 196–210, http://dx.doi.org/10.1002/qj.2645.

[24] H. Joos, R.M. Forbes, Impact of different IFS microphysics on a warm conveyor belt and the downstream flow evolution, Q. J. R. Meteorol. Soc. 142 (700) (2016) 2727–2739, http://dx.doi.org/10.1002/qj.2863.

[25] M. Mazoyer, D. Ricard, G. Rivière, J. Delanoë, P. Arbogast, B. Vié, C. Lac, Q. Cazenave, J. Pelon, Microphysics Impacts on the Warm Conveyor Belt and Ridge Building of the NAWDEX IOP6 Cyclone, Mon. Weather Rev. 149 (12) (2021) 3961–3980, http://dx.doi.org/10.1175/MWR-D-21-0061.1.

[26] M. Mazoyer, D. Ricard, G. Rivière, J. Delanoë, S. Riette, C. Augros, M. Borderies, B. Vié, Impact of mixed-phase cloud parameterization on warm conveyor belts and upper-tropospheric dynamics, Mon. Weather Rev. 151 (5) (2023) 1073–1091, http://dx.doi.org/10.1175/MWR-D-22-0045.1.

[27] M. Pickl, S.T.K. Lang, M. Leutbecher, C.M. Grams, The effect of stochastically perturbed parametrisation tendencies (SPPT) on rapidly ascending air streams, Q. J. R. Meteorol. Soc. 148 (744) (2022) 1242–1261, http://dx.doi.org/10.1002/qj.4257.

[28] D. Steinfeld, M. Boettcher, R. Forbes, S. Pfahl, The sensitivity of atmospheric blocking to upstream latent heating – numerical experiments, WCD 1 (2) (2020) 405–426, http://dx.doi.org/10.5194/wcd-1-405-2020.

[29] A. Schäfler, F. Harnisch, Impact of the inflow moisture on the evolution of a warm conveyor belt, Q. J. R. Meteorol. Soc. 141 (686) (2015) 299–310, http://dx.doi.org/10.1002/qj.2360.

[30] F. Zhang, N. Bei, R. Rotunno, C. Snyder, C.C. Epifanio, Mesoscale Predictability of Moist Baroclinic Waves: Convection-Permitting Experiments and Multistage Error Growth Dynamics, J. Atmos. Sci. 64 (10) (2007) 3579–3594, http://dx.doi.org/10.1175/JAS4028.1.

[31] C.M. Grams, L. Magnusson, E. Madonna, An atmospheric dynamics perspective on the amplification and propagation of forecast error in numerical weather prediction models: A case study, Q. J. R. Meteorol. Soc. 144 (717) (2018) 2577–2591, http://dx.doi.org/10.1002/qj.3353.

[32] H. Joos, H. Wernli, Influence of microphysical processes on the potential vorticity development in a warm conveyor belt: A case-study with the limited-area model COSMO, Q. J. R. Meteorol. Soc. 138 (663) (2012) 407–418, http://dx.doi.org/10.1002/qj.934.

[33] A. Oertel, A.K. Miltenberger, C.M. Grams, C. Hoose, Interaction of microphysics and dynamics in a warm conveyor belt simulated with the ICOsahedral Non-hydrostatic (ICON) model, Atmos. Chem. Phys. 23 (15) (2023) 8553–8581, http://dx.doi.org/10.5194/acp-23-8553-2023.

[34] J. Fan, Y. Wang, D. Rosenfeld, X. Liu, Review of aerosol–cloud interactions: Mechanisms, significance, and challenges, J. Atmos. Sci. 73 (11) (2016) 4221–4252, http://dx.doi.org/10.1175/JAS-D-16-0037.1.

[35] C. Wellmann, A.I. Barrett, J.S. Johnson, M. Kunz, B. Vogel, K.S. Carslaw, C. Hoose, Using emulators to understand the sensitivity of deep convective clouds and hail to environmental conditions, J. Adv. Model. Earth Syst. 10 (2018) 3103–3122, http://dx.doi.org/10.1029/2018MS001465.

[36] A.L. Igel, S.C. van den Heever, Invigoration or enervation of convective clouds by aerosols? Geophys. Res. Lett. 48 (2021) http://dx.doi.org/10.1029/2021GL093804, e2021GL093804.

[37] C. Barthlott, A. Zarboo, T. Matsunobu, C. Keil, Importance of aerosols and shape of the cloud droplet size distribution for convective clouds and precipitation, Atmos. Chem. Phys. 22 (2022) 2153–2172, http://dx.doi.org/10.5194/acp-22-2153-2022.

[38] T. Matsunobu, C. Keil, C. Barthlott, The impact of microphysical uncertainty conditional on initial and boundary condition uncertainty under varying synoptic control, Weather. Clim. Dyn. 3 (4) (2022) 1273–1289, http://dx.doi.org/10.5194/wcd-3-1273-2022, URL https://wcd.copernicus.org/articles/3/1273/2022/.

[39] R.M. Forbes, P.A. Clark, Sensitivity of extratropical cyclone mesoscale structure to the parametrization of ice microphysical processes, Q. J. R. Meteorol. Soc. 129 (589) (2003) 1123–1148, http://dx.doi.org/10.1256/qj.01.171.

[40] H. Joos, E. Madonna, K. Witlox, S. Ferrachat, H. Wernli, U. Lohmann, Effect of anthropogenic aerosol emissions on precipitation in warm conveyor belts in the western North Pacific in winter – a model study with ECHAM6-HAM, Atmos. Chem. Phys. 17 (10) (2017) 6243–6255, http://dx.doi.org/10.5194/acp-17-6243-2017.

[41] A. Seifert, K.D. Beheng, A two-moment cloud microphysics parameterization for mixed-phase clouds. Part 1: Model description, Meteorol. Atmos. Phys. 92 (1–2) (2006) 45–66, http://dx.doi.org/10.1007/s00703-005-0112-4.

[42] A. Seifert, On the Parameterization of Evaporation of Raindrops as Simulated by a One-Dimensional Rainshaft Model, J. Atmos. Sci. 65 (11) (2008) 3608–3619, http://dx.doi.org/10.1175/2008JAS2586.1.

[43] G. Zängl, D. Reinert, P. Rípodas, M. Baldauf, The ICON (ICOsahedral Non-hydrostatic) modelling framework of DWD and MPI-M : Description of the non-hydrostatic dynamical core, Q. J. R. Meteorol. Soc. 141 (687) (2015) 563–579, http://dx.doi.org/10.1002/qj.2378.

[44] M. Tiedtke, A comprehensive mass flux scheme for cumulus parameterization in large-scale models, Mon. Weather Rev. 117 (1989) 1779–1800, http://dx.doi.org/10.1175/1520-0493(1989)117,1779:ACMFSF.2.0.CO;2.

[45] P. Bechtold, M. Köhler, T. Jung, F. Doblas-Reyes, M. Leutbecher, M.J. Rodwell, F. Vitart, G. Balsamo, Advances in simulating atmospheric variability with the ECMWF model: From synoptic to decadal time-scales, Q. J. R. Meteorol. Soc. 134 (2008) 1337–1351, http://dx.doi.org/10.1002/qj.289.

[46] ECMWF, IFS Documentation CY41R2 - Part III: Dynamics and Numerical Procedures, ECMWF, 2016, pp. 12–14, http://dx.doi.org/10.21957/83wouv80, 3, URL https://www.ecmwf.int/node/16647.

[47] M. Raschendorfer, The new turbulence parameterization of LM, 2018, pp. 89–97, COSMO News Letter No. 1, Consortium for Small-Scale Modelling.

[48] F. Lott, M.J. Miller, A new subgrid-scale orographic drag parametrization: Its formulation and testing, Q. J. R. Meteorol. Soc. 123 (1997) 101–127, http://dx.doi.org/10.1002/qj.49712353704.

[49] A. Orr, P. Bechtold, J. Scinocca, M. Ern, M. Janiskova, Improved middle atmosphere climate and forecasts in the ECMWF model through a nonorographic gravity wave drag parameterization, J. Clim. 23 (2010) 5905–5926, http://dx.doi.org/10.1175/2010JCLI3490.

[50] R.J. Hogan, A. Bozzo, ECRAD: A New Radiation Scheme for the IFS, European Centre for Medium-Range Weather Forecasts, 2016.

[51] A.K. Miltenberger, T. Lüttmer, C. Siewert, Secondary ice formation in idealised deep convection - Source of primary ice and impact on glaciation, Atmosphere 11 (5) (2020) http://dx.doi.org/10.3390/atmos11050542.

[52] A. Oertel, M. Boettcher, H. Joos, M. Sprenger, H. Konow, M. Hagen, H. Wernli, Convective activity in an extratropical cyclone and its warm conveyor belt – a case-study combining observations and a convection-permitting model simulation, Q. J. R. Meteorol. Soc. 145 (721) (2019) 1406–1426, http://dx.doi.org/10.1002/qj.3500.

[53] A. Oertel, M. Sprenger, H. Joos, M. Boettcher, H. Konow, M. Hagen, H. Wernli, Observations and simulation of intense convection embedded in a warm conveyor belt – how ambient vertical wind shear determines the dynamical impact, WCD 2 (1) (2021) 89–110, http://dx.doi.org/10.5194/wcd-2-89-2021.

[54] A. Schäfler, M. Boettcher, C. Grams, M. Rautenhaus, H. Sodemann, H. Wernli, Planning aircraft measurements within a warm conveyor belt, Weather (69) (2014) 161–166.

[55] J.F. Quinting, C.M. Grams, EuLerian Identification of ascending AirStreams (ELIAS 2.0) in numerical weather prediction and climate models – Part 1: Development of deep learning model, Geosci. Model. Dev. 15 (2) (2022) 715–730, http://dx.doi.org/10.5194/gmd-15-715-2022.

[56] J.F. Quinting, C.M. Grams, A. Oertel, M. Pickl, EuLerian Identification of ascending AirStreams (ELIAS 2.0) in numerical weather prediction and climate models – Part 2: Model application to different datasets, Geosci. Model. Dev. 15 (2) (2022) 731–744, http://dx.doi.org/10.5194/gmd-15-731-2022.

[57] C. Schwenk, A. Miltenberger, The role of ascent timescale for WCB moisture transport into the UTLS, 2024, http://dx.doi.org/10.5194/egusphere-2024-2402,

[58] M. Baumgartner, M. Sagebaum, N.R. Gauger, P. Spichtinger, A. Brinkmann, Algorithmic differentiation for cloud schemes (IFS Cy43r3) using CoDiPack (v1.8.1), Geosci. Model. Dev. 12 (12) (2019) 5197–5212, http://dx.doi.org/10.5194/gmd-12-5197-2019.

[59] A. Oertel, M. Boettcher, H. Joos, M. Sprenger, H. Wernli, Potential vorticity structure of embedded convection in a warm conveyor belt and its relevance for large-scale dynamics, WCD 1 (1) (2020) 127–153, http://dx.doi.org/10.5194/wcd-1-127-2020.

[60] M. Hieronymus, A. Oertel, WCB Trajectories with Sensitivities to Cloud Microphysical Parameters (North Atlantic Region in Early October 2016), Zenodo, 2024, http://dx.doi.org/10.5281/ZENODO.13920285.

[61] L.B. Hande, C. Engler, C. Hoose, I. Tegen, Parameterizing cloud condensation nuclei concentrations during HOPE, Atmos. Chem. Phys. 16 (18) (2016) 12059–12079, http://dx.doi.org/10.5194/acp-16-12059-2016.

[62] M. Hieronymus, Wavestoweather/AD_Sensitivity_Analysis: V2.3, Zenodo, 2024, http://dx.doi.org/10.5281/ZENODO.13920256.

Maicon Hieronymus is a Ph.D. candidate at Johannes Gutenberg University Mainz, where he began his doctoral studies in 2019 in collaboration with the Waves to Weather project, funded by the German Science Foundation (DFG). He received his B.Sc. and M.Sc. degrees in computer science with an emphasis on experimental physics from the Johannes Gutenberg University Mainz, Germany. His current research interests are automatic differentiation of models in atmosphere physics, aimed at enabling computationally efficient sensitivity analysis of cloud microphysics with an emphasis on fast-ascending parcels within the warm conveyor belt.

Annika Oertel is a Young Investigator Group leader at KIT, Germany, since 2023. She received her Ph.D. in atmospheric dynamics in 2019 from ETH Zurich, Switzerland, and has worked as postdoctoral researcher at ETH and KIT between 2020 and 2023. Since 2024, she is editor for Atmospheric Chemistry and Physics. Her research interests include modeling of mid-latitude atmospheric processes across scales ranging from the micro- to the synoptic scale, interactions between scales, as well as synergistic analysis of numerical weather prediction model data and observations.

Annette K. Miltenberger is a junior professor at the Institute for Atmospheric Physics of JGU since 2023. She received her Ph.D. in atmospheric dynamics in 2014 from ETH Zurich, Switzerland, and has worked as research fellow at the University of Leeds, UK, and JGU, Germany, between 2014 and 2023. Since 2024 she is associated editor of the Quarterly Journal of the Royal Meteorological Society and a member of the International Commission on Clouds and Precipitation executive committee. Her research focusses on the interaction between atmospheric flow, clouds and aerosols, which her group explores with numerical models of varying complexity and observational data.

André Brinkmann is a full professor at the computer science department of JGU (since 2011). He was the head of the data center at the Johannes Gutenberg University from 2011 until 2021. He received his Ph.D. in electrical engineering in 2004 from Paderborn University and was an assistant professor in the computer science department of Paderborn University from 2008 to 2011. Furthermore, he was the managing director of the Paderborn Center for Parallel Computing PC2 during this time frame. His research interests focus on the application of algorithm engineering techniques in the area of data center management, cloud computing, and storage systems. He has published more than 150 papers in renowned conferences and journals and is a senior associated editor of the ACM Transactions on Storage.